CrossMark

J. Fluid Mech. (2021), *vol*. 909, A3. © The Author(s), 2020.
Published by Cambridge University Press
doi:10.1017/jfm.2020.851

Jetting in finite-amplitude, free, capillary-gravity waves

Saswata Basak[1], **Palas Kumar Farsoiya**[1] **and Ratul Dasgupta**[1],†

[1]Department of Chemical Engineering, Indian Institute of Technology Bombay, Powai, Mumbai 400 076, India

(Received 28 March 2020; revised 13 June 2020; accepted 4 October 2020)

We present a theoretical and computational study of the mechanics of a jet formed from a large amplitude, axisymmetric, capillary-gravity wave on the surface of a liquid pool in a cylindrical container. Jetting can cause a pronounced overshoot of the interface at the axis of symmetry. A linear theory presented earlier in Farsoiya *et al.* (*J. Fluid Mech.*, vol. 826, 2017, pp. 797–818) was shown to be incapable of describing this jet. To understand its mechanics, we present here the inviscid, weakly nonlinear solution to the initial value problem where the initial surface perturbation is a single Fourier–Bessel mode on quiescent fluid. The theory predicts that energy injected into a primary (Bessel) mode initially is transferred nonlinearly to a spectrum of modes. The extent of the theoretically predicted energy transfer is found to be very accurate for modes up to the second harmonic. We show using numerical simulations that the jet originates as a small dimple formed at the trough of the wave, analogous to similar observations in bubble cavity collapse (Duchemin *et al.*, *Phys. Fluids*, vol. 14, 2002, pp. 3000–3008; Lai *et al.*, *Phys. Rev. Lett.* vol. 121, 2018, 144501). The theory is able to describe the jet overshoot and the velocity and pressure fields in the liquid qualitatively, but does not capture the temporal evolution of the dimple or the thinning of the jet neck leading to pinchoff. Modal analysis shows that the latter phenomenon requires higher-order approximations, beyond the second order presented here. The nonlinear theory yields explicit analytical expressions without any fitting parameters which are systematically tested against numerical simulations of the incompressible Euler equation. The theory contains cylindrical analogues of the singularities corresponding to second harmonic resonance (Wilton, *Lond. Edinb. Dubl. Phil. Mag. J. Sci.*, vol. 29, 1915, pp. 688–700). The connection of these to triadic resonant interactions among capillary-gravity waves in a cylindrical confined geometry is discussed.

Key words: capillary waves, surface gravity waves

1. Introduction

Formation of an axisymmetric or two-dimensional liquid jet due to the collapse of an air cavity is a well-documented phenomenon which may be observed in a wide range of natural or engineered situations (MacIntyre 1972; Tsai *et al.* 2017; Lai, Eggers & Deike 2018). Understanding the mechanics of these jets from first principles is a challenging

† Email address for correspondence: dasgupta.ratul@iitb.ac.in

https://doi.org/10.1017/jfm.2020.851 Published online by Cambridge University Press

problem and progress in this accrues benefit for various scientific and engineering applications. For example, these jets may be produced from collapsing bubbles near a solid wall, and being able to control their direction of ejection is a significant step in preventing erosion damage to turbomachinery surfaces (Blake & Gibson 1981). Bursting bubbles at the ocean surface (Veron 2015) or those in a glass of champagne (Ghabache *et al.* 2014*a*) generate air cavities which collapse producing similar liquid jets which can release drops from their tip (Duchemin *et al.* 2002; Gordillo & Gekle 2010; Gañán-Calvo 2017, 2018*b*). At the ocean surface, these ejected drops constitute an important source of sea-salt aerosols (Kientzler *et al.* 1954; Veron 2015) while those in the champagne glass assist in the spread of aroma (Liger-Belair *et al.* 2009; Ghabache *et al.* 2014*a*; Ghabache & Séon 2016; Séon & Liger-Belair 2017). Similar jets are observed at the base of a collapsing cavity in overdriven Faraday waves (Longuet-Higgins 1983; Zeff *et al.* 2000) and play a crucial role in vibration-induced atomisation of droplets (Goodridge, Hentschel & Lathrop 1999; James *et al.* 2003; Tsai *et al.* 2017). They are also formed during sloshing and atomisation (Das & Hopfinger 2008; Raja, Das & Hopfinger 2019) occurring inside fuel-filled containers subjected to vibrations. Yet other examples include jets formed when a droplet impacts a liquid pool (Prosperetti & Oguz 1993; Morton, Rudman & Jong-Leng 2000; Bartolo, Josserand & Bonn 2006; Ray, Biswas & Sharma 2015), 'Worthington jets' produced through water entry of projectiles (Worthington & Cole 1897, 1900; Gordillo 2008; Gekle & Gordillo 2010; Truscott, Epps & Belden 2014) or the so-called 'Pokrovski's experiment' (Milgram 1969; Antkowiak *et al.* 2007; Yukisada *et al.* 2018) where a column of liquid in a container is allowed to fall freely and, following impact with the floor, a liquid jet shoots upwards at the centre of the container. A list of various situations of occurrence of these jets has been enumerated in Gekle & Gordillo (2010) and pictorially in Ganán-Calvo & Lopez-Herrera (2019).

In a recent study (Farsoiya, Mayya & Dasgupta 2017), we have shown using direct numerical simulations that jets can be obtained from free, large amplitude interfacial oscillations. Perturbing the interface as a Bessel function (see figure 1*a*), it was found that jetting and droplet ejection are obtained at the axis of symmetry, as the non-dimensional parameter $\epsilon \equiv a_0 k$ (also known as the wave steepness parameter in classical water-wave theory, see figure 1(*b*), Lake & Yuen (1977) and Longuet-Higgins (1978)) is systematically increased. The complete inability of the linear initial value problem (IVP) to model these jets was demonstrated in Farsoiya *et al.* (2017). The aim of the present study is to report significant progress made in the understanding and modelling of these jets since our 2017 study. Notably, we show here that these jets can be obtained from the inviscid equations of motion (in contrast to the viscous equations solved earlier in Farsoiya *et al.* (2017)). We also demonstrate here that the inception of these jets closely mimic those seen in Faraday waves, bursting bubbles and many other scenarios. A novel weakly nonlinear solution (up to $O(\epsilon^2)$) to the IVP is then presented for modelling the jets. In the next paragraph, we describe the qualitative phenomenology of the formation of these jets in the current study.

The phenomenology of jetting is depicted in figure 2(*a–c*) (also see accompanying file Movie.mp4 available at https://doi.org/10.1017/jfm.2020.851). The time evolution of the interface starting with a single Bessel mode (see figure 1*a*) is obtained from numerical simulations of the axisymmetric Euler equation. Figures 2(*a*), 2(*b*) and 2(*c*) correspond to moderate and large values of ϵ and depict the interface shape at various times. In figure 2(*a*), at time $\hat{t} = 0.020$ s, a dimple-like structure appears around $\hat{r} = 0$. It gets momentarily suppressed at $\hat{t} = 0.027$ s, before reappearing as a more pronounced dimple at $\hat{t} = 0.051$ s (see right-hand inset) with associated curvature reversal similar to what is also known in bubble bursting (Deike *et al.* 2018; Ganán-Calvo & Lopez-Herrera 2019).

https://doi.org/10.1017/jfm.2020.851 Published online by Cambridge University Press

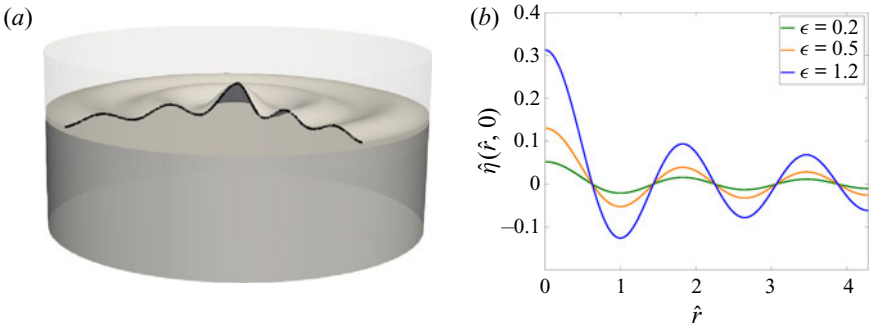

FIGURE 1. (*a*) Initial condition: the black line depicts cross-section of the perturbed interface at $\hat{t} = 0$. The interface initially is $\hat{\eta}(\hat{r}, 0) = a_0 \mathrm{J}_0(k\hat{r})$ where J_0 is the zeroth-order Bessel function of the first kind, k is the wavenumber, a_0 is the perturbation amplitude and $\hat{r}$ is the radial coordinate. The liquid (in grey) is quiescent initially. (*b*) The effect of changing the wave steepness parameter $\epsilon \equiv a_0 k$ on the initial perturbation. Here ϵ is a non-dimensional measure of the maximum slope of the initial perturbation. A wave with $\epsilon \ll 1$ has an amplitude much smaller than its wavelength and can be described by linear theory. Jets form at the axis of symmetry for moderate to high values of ϵ (>0.5 typically) and are nonlinear phenomena. We use ϵ as a small parameter in our perturbative expansion.

The formation of this dimple is a nonlinear event and constitutes the first signature of impending jet formation. More features are seen in figures 2(*b*) and 2(*c*) where ϵ is higher. The jet is clearly visible and is seen to rise to a height greater than the maximum height of the perturbation at $\hat{t} = 0$, *viz.* an overshoot at $\hat{r} = 0$ is observed. In figure 2(*c*) the formation of a slender jet with the ejection of a droplet from its tip is seen. This jetting seen here from free interfacial oscillations bears a qualitative resemblance to that observed during cavity collapse in bubble bursting (see Gekle & Gordillo 2010; Kroon 2012; Gañán-Calvo 2017; Lai *et al.* 2018). We present a short review of the jetting literature below, focussing on analytical models and simulations. A classification of the literature on the various jetting scenarios is also provided in table 1.

1.1. *Literature review: analytical models and simulations*

Analytical solutions related to jetting have focussed on the surface singularity due to divergence of local curvature (Longuet-Higgins 1983; Zeff *et al.* 2000) or the surface itself (Goodridge, Shi & Lathrop 1996; Shi, Goodridge & Lathrop 1997; Hogrefe *et al.* 1998). Related studies include self-similar solutions close to the singularity (Zeff *et al.* 2000; Duchemin *et al.* 2002) and scaling analysis (Duchemin *et al.* 2002; Gañán-Calvo 2017; Lai *et al.* 2018). An early attempt at modelling these axisymmetric jets was by Longuet-Higgins (1983) who discovered a solution to the axisymmetric Laplace equation with a time-varying free surface. The free surface becoming orthogonal to the streamlines everywhere is a singularity in this model, identified with the onset of jetting (Longuet-Higgins 1994). While good quantitative agreement was obtained between the model and bubble collapse data of Blake & Gibson (1981), the agreement with the author's experiments for jets in overdriven Faraday waves was qualitative. A notable analytical and experimental study of jetting in Faraday waves was reported by Zeff *et al.* (2000) who argued that the singularity implied by Longuet-Higgins (1983) is concomitant with a change in surface topology, leading to entrapment of a bubble.

https://doi.org/10.1017/jfm.2020.851 Published online by Cambridge University Press

https://doi.org/10.1017/jfm.2020.851 Published online by Cambridge University Press

Literature on jet formation (T, theory; S, simulations; E, experiments)

Faraday waves	**Bursting bubbles at a free surface**	**Water entry of projectiles**	**Drop impact on a pool**	**Other scenarios**
Longuet-Higgins (1983) **(E,T)**	Blanchard (1963), Blanchard & Syzdek (1972), Blanchard (1989), Blanchard (2004) **(E)**	Worthington & Cole (1897), Worthington & Cole (1900) **(E)**	Prosperetti & Oguz (1993) **(Review)**	Blake & Gibson (1981) (**Cavitation**)
Longuet-Higgins (1994) **(T)**	Woodcock *et al.* (1953) **(E)**	Cheny & Walters (1996) **(E)**	Morton *et al.* (2000) **(S,E)**	Antkowiak *et al.* (2007) (**Pokrovski experiment,T,E**)
Zeff *et al.* (2000) **(E,T)**	MacIntyre (1972) **(E,T)**	Shin & McMahon (1990) **(E)**	Bartolo *et al.* (2006) **(E)**	Thoroddsen, Etoh & Takehara (2007) **(Oscillating drops, E)**
Goodridge *et al.* (1996), Hogrefe *et al.* (1998), Goodridge *et al.* (1999) **(T,E)**	Duchemin *et al.* (2002) **(S,T)**	Gekle *et al.* (2009), Gekle & Gordillo (2010) **(E,T,S)**	Ray *et al.* (2015) **(S)**	Tjan & Phillips (2007) **(Jetting in lungs, S,T)**
James *et al.* (2003) **(E,T)**	Ghabache, Séon & Antkowiak (2014*b*), Ghabache *et al.* (2014*a*), Ghabache & Séon (2016), Krishnan, Hopfinger & Puthenveettil (2017) **(T,E)**	Truscott *et al.* (2014) **(Review)**	Thoroddsen *et al.* (2018) **(E)**	Ghabache *et al.* (2014*b*) **(Cavity collapse, T,E)**

TABLE 1. See Caption on next page.

https://doi.org/10.1017/jfm.2020.851 Published online by Cambridge University Press

Das & Hopfinger (2008) **(T,E)**	Lai *et al.* (2018), Deike *et al.* (2018) **(S,T)**	Kim & Park (2019) **(E)**	Yamamoto, Motosuke & Ogata (2018) **(E)**	Farsoiya *et al.* (2017) **(Capillary-gravity waves, T,S)**
Tsai *et al.* (2017) **(E)**	Gañán-Calvo (2017), Gañán-Calvo (2018*a*), Gañán-Calvo (2018*b*), Ganán-Calvo & Lopez-Herrera (2019) **(T)**	—	Castillo-Orozco *et al.* (2015) **(E,S)**	van Rijn (2018) **(Various cases, T,E)**
Raja *et al.* (2019) **(T,E)**	Gordillo & Rodríguez-Rodríguez (2018), Gordillo & Rodríguez-Rodríguez (2019), Kang & Cho (2019), Blanco-Rodríguez & Gordillo (2020) **(T,S)**	—	—	Ismail *et al.* (2018) (**Cavity collapse, T,S**)

TABLE 1. The literature covering various jetting scenarios.

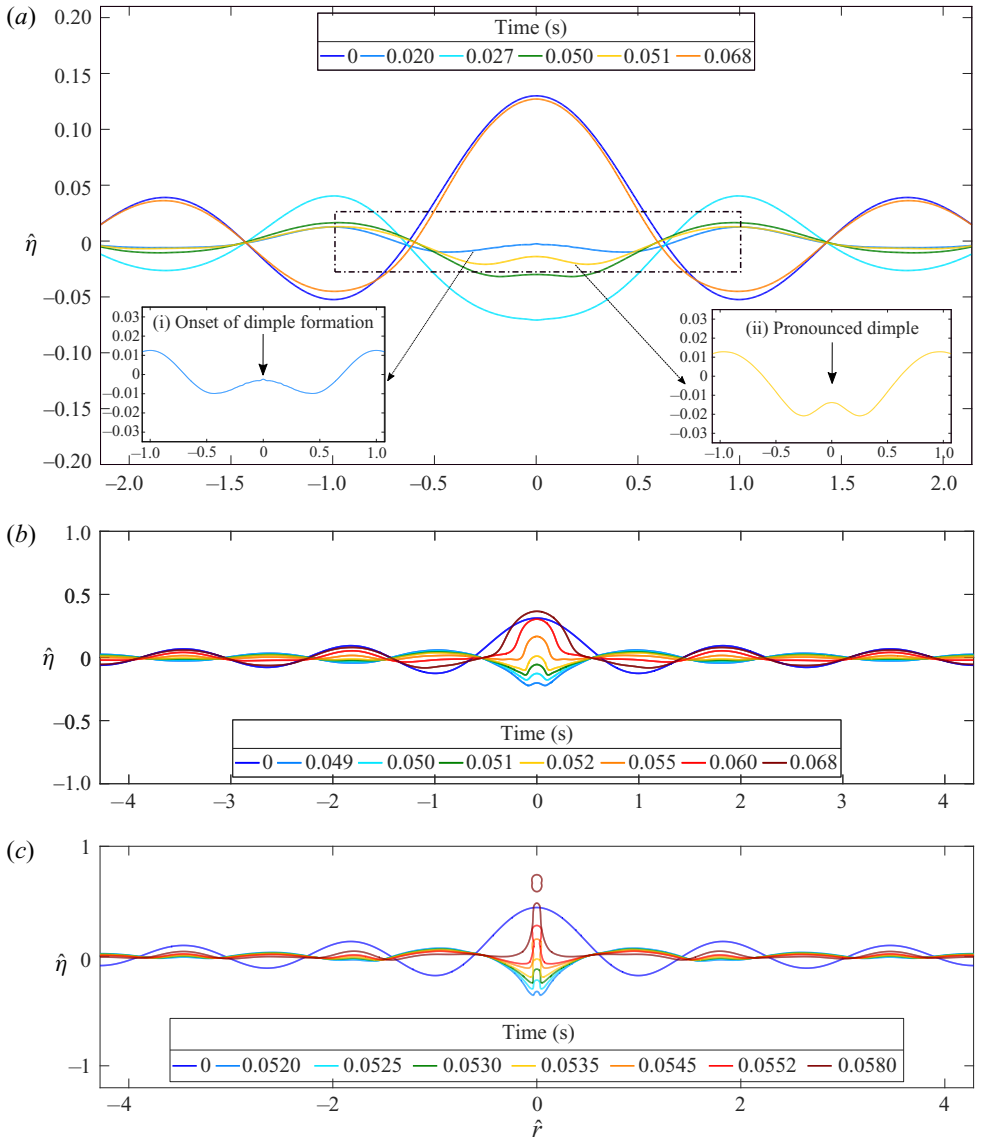

FIGURE 2. Results from numerical simulations: temporal evolution of the interface for (*a*) $\epsilon = 0.5$, (*b*) $\epsilon = 1.2$ and (*c*) $\epsilon = 1.7$. (*a*) A dimple appearing at the base of the wave trough is a nonlinear event and signals impending jetting. This is seen more clearly in panels (*b*,*c*) where ϵ is chosen to be larger and produces a jet which overshoots the initial perturbation at $\hat{r} = 0$ and also ejects a drop in panel (*c*); note the slender jet. (*a*) Dimple formation with time for $\epsilon = 0.5$. (*b*) Pronounced dimple, jet formation and overshoot at $\hat{r} = 0$ for $\epsilon = 1.2$. (*c*) Pronounced dimple, slender jet, overshoot, drop ejection for $\epsilon = 1.7$.

Sufficiently close to the singularity, Zeff *et al.* (2000) proposed a similarity solution where it was suggested that due to divergence of curvature and surface velocities, gravity is unimportant and the surface profile is determined by a balance between nonlinear inertia and surface tension. The first well-resolved numerical experiment (solving the Navier–Stokes equations) demonstrating jetting from bubble bursting was by

https://doi.org/10.1017/jfm.2020.851 Published online by Cambridge University Press

Duchemin *et al.* (2002). They clearly showed the focussing of capillary waves leading to dimple and jet formation. In addition, they also demonstrated the validity of the self-similar nature of the cavity collapse and the existence of an optimal viscosity where the jet velocity was maximum. A set of studies by Gekle *et al.* (2009) and Gekle & Gordillo (2010) have shown that the Longuet-Higgins model is inadequate for jets generated in disk entry into a liquid pool. Modelling the flow due to a collapsing cavity using a line of sinks (Gekle *et al.* 2009), the authors obtained good agreement for the time evolution of the base coordinates with simulations and experiments. Gekle & Gordillo (2010) also further elucidated the structure of their jets demonstrating good agreement with simulations and model predictions for the jet shape.

The current consensus in the literature is that that the inception of these jets is due to focussing of capillary waves at the axis of symmetry (MacIntyre 1972; Duchemin *et al.* 2002). The detailed physical mechanism of this focussing has been under active debate recently, in particular the role of viscosity in this focussing process as well as the dominant wavelength which gets focussed (Duchemin *et al.* 2002; Gañán-Calvo 2017; Lai *et al.* 2018; Gañán-Calvo 2018*a*; Gordillo & Rodríguez-Rodríguez 2018). A number of numerical simulations on jetting through bursting bubbles or Faraday waves have utilised the inviscid, irrotational framework employing the boundary integral technique (Boulton-Stone & Blake 1993; Gekle & Gordillo 2010). Since the seminal study by Duchemin *et al.* (2002), many studies have been reported where the full Navier–Stokes equations with an interface or a free-surface have been solved, capturing jet formation with high resolution (Ray *et al.* 2015; Deike *et al.* 2018; Lai *et al.* 2018; Blanco-Rodríguez & Gordillo 2020). Predicting the rate and size of droplets from these jets have important applications, e.g. see Blanco-Rodríguez & Gordillo (2020) and the important recent study by Ismail *et al.* (2018) which has elucidated, via experiments and simulations, the criterion for minimising the size and number of ejected droplets from jetting obtained from cavity collapse, in addition to providing scaling laws for the size of drops.

While time-periodic, large-amplitude gravity waves in cylindrical geometry have been studied in Mack (1962) and Fultz & Murty (1963), solution to the IVP is far less explored. To the best of our knowledge, there have been only two studies using the IVP approach in cylindrical axisymmetric geometry. The study by Jacobs & Catton (1988) solved the weakly nonlinear IVP in a generalised framework in a number of geometries, focussing on nonlinear corrections to the cutoff wavenumber for the Rayleigh–Taylor instability. They did not discuss the application of their results to jetting or comment on the presence of critical points due to triadic resonant interactions. A more recent linearised IVP approach has been the study by Kang & Cho (2019) which has experimentally investigated capillary-gravity waves from the bursting of a bubble underwater. The analytical part of this study was confined to the linearised regime *viz.* the axisymmetric Cauchy–Poisson solution (Debnath 1994), which cannot describe jetting.

1.2. *Utility of the IVP approach*

It is clear that the nonlinear IVP approach has not been employed to study jetting. As we show, this approach coupled with modal decomposition of the interface provides insight into the mechanics. In our simulations we inject the total initial (potential) energy into a single mode, labelled the primary mode. By systematically increasing ϵ for this mode, we obtain dimple formation and jetting. Modal analysis of the dimple and the jet shape at its maximum overshoot, shows that when these occur, a part of the initial (potential) energy in the primary mode gets transferred to other modes. Clearly, this cannot occur through a linear mechanism which prohibits any intermodal energy transfer. The weakly nonlinear

https://doi.org/10.1017/jfm.2020.851 Published online by Cambridge University Press

IVP solution overcomes this limitation of linear theory by allowing for energy transfer among modes. We show that while the pressure, velocity fields, inception of dimple and maximum overshoot of the jet are qualitatively captured by our second-order theory, the surface velocity and the temporal evolution of the pronounced dimple and the thinning of the jet leading to pinchoff are not, and resolving these require higher-order corrections. The aforementioned insights obtained through a first principles IVP approach are novel and complement prior seminal studies investigating the problem from a wave-focussing, singularity formation, self-similarity and scaling perspective, cf. MacIntyre (1972), Zeff *et al.* (2000), Duchemin *et al.* (2002), Gordillo (2008), Gañán-Calvo (2017), Gordillo & Rodríguez-Rodríguez (2018), Lai *et al.* (2018), Ismail *et al.* (2018) and Blanco-Rodríguez & Gordillo (2020).

Our study is organised as follows. We present the weakly nonlinear solution in § 2. In § 3, we describe numerical simulations followed by § 4 where analytical predictions are compared with simulations. Section 5 discusses energy conservation and surface energy redistribution through modal analysis. Section 6 discusses the singular values of σ (inverse Bond number) in our theory connecting these to triadic resonant interactions among capillary-gravity waves in a cylindrical confined geometry.

2. Weakly nonlinear solution

2.1. *Governing equations*

Figure 3 shows a cylindrical container of radius $\hat{R}_0$ containing fluid whose surface is perturbed in the form of a Bessel mode. The displacement of the perturbed surface is measured from the flat undisturbed level and is given initially by $\hat{\eta}(\hat{r}, 0) = a_0 \mathrm{J}_0(k\hat{r}) = a_0 \mathrm{J}_0((l_q/\hat{R}_0)\hat{r})$ where J_0 is the zeroth-order Bessel function of first kind and l_q is explained below (2.6*a*,*b*). Surface oscillations arise due to the initial perturbation, and for a sufficiently large value of $\epsilon \equiv a_0(l_q/\hat{R}_0)$ (the precise value depends on the non-dimensional number σ), a jet is formed at the axis of symmetry towards the end of a surface oscillation. We study the IVP corresponding to this surface perturbation under the inviscid, irrotational approximation. Here we assume the liquid to be water and the gas above it to be air. Due to the large density ratio between the two, we may safely ignore the dynamic effect of air assuming that it exerts negligible pressure on the water surface. Thus the interface is treated as a free surface with a pressure jump across it due to surface tension.

The Laplace equation along with the nonlinear boundary conditions (kinematic boundary condition (2.2) and the Bernoulli equation with surface tension (2.3)) at the free surface and the mass conservation condition (2.4) govern the perturbation velocity potential and the perturbed interface. Equations for these are

$$\hat{\boldsymbol{\nabla}} \cdot \hat{\boldsymbol{\nabla}} \hat{\phi} = 0, \tag{2.1}$$

$$\frac{\mathrm{D}\hat{\eta}}{\mathrm{D}\hat{t}} - \left(\hat{\boldsymbol{\nabla}} \hat{\phi} \cdot \boldsymbol{e}_{\hat{z}} \right)_{\hat{z}=\hat{\eta}} = 0, \tag{2.2}$$

$$\left(\frac{\partial \hat{\phi}}{\partial \hat{t}} + \frac{1}{2} |\hat{\boldsymbol{\nabla}} \hat{\phi}|^2 + g\hat{z} + \frac{T}{\rho} \hat{\boldsymbol{\nabla}} \cdot \boldsymbol{n} \right)_{\hat{z}=\hat{\eta}} = 0, \tag{2.3}$$

$$\int_0^{\hat{R}_0} \hat{r}\hat{\eta}(\hat{r}, \hat{t}) \, \mathrm{d}\hat{r} = 0, \tag{2.4}$$

https://doi.org/10.1017/jfm.2020.851 Published online by Cambridge University Press

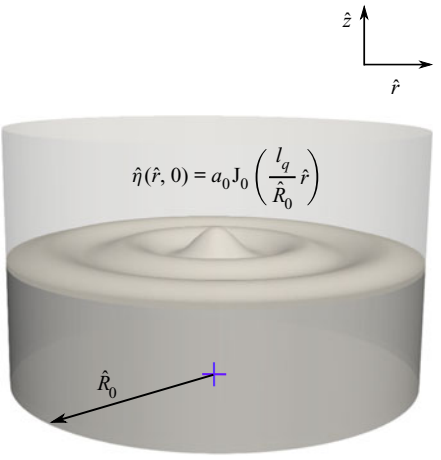

FIGURE 3. Three-dimensional visualisation of surface perturbation (grey). Surface perturbation imposed at $\hat{t} = 0$ leads to a jet at the end of one oscillation for sufficiently large ϵ. The coordinate system is centred at the axis of symmetry and $\hat{z}$ is measured from the unperturbed free surface.

where T is the coefficient of surface tension, $\boldsymbol{e}_{\hat{z}}$ and $\boldsymbol{n}$ are unit normals to the unperturbed and perturbed free surface, respectively, and $\hat{\boldsymbol{\nabla}}$ is the gradient operator to be expressed in axisymmetric, cylindrical coordinates. We propose to solve the nonlinear IVP for (2.1), (2.2) and (2.3) up to $O(\epsilon^2)$ in cylindrical coordinates with an imposed surface perturbation (see figure 3 and (2.6*a*,*b*)). Appropriate boundary conditions are imposed on the velocity potential $\hat{\phi}$ at the axis of symmetry ($\hat{r} = 0$) and the wall of the container at $\hat{r} = \hat{R}_0$ (no-penetration). In addition, we impose symmetry conditions on the free-surface at $\hat{r} = 0$ as well as the free-end edge boundary condition at $\hat{r} = \hat{R}_0$ through (2.5*a*,*b*);

$$\left(\frac{\partial\hat{\phi}}{\partial\hat{r}}\right)_{\hat{r}=0} = \left(\frac{\partial\hat{\phi}}{\partial\hat{r}}\right)_{\hat{r}=\hat{R}_0} = 0, \quad \left(\frac{\partial\hat{\eta}}{\partial\hat{r}}\right)_{\hat{r}=0} = \left(\frac{\partial\hat{\eta}}{\partial\hat{r}}\right)_{\hat{r}=\hat{R}_0} = 0, \tag{2.5a,b}$$

$$\hat{\eta}(\hat{r},0) = a_0 \mathrm{J}_0\left(\frac{l_q}{\hat{R}_0}\hat{r}\right), \quad \frac{\partial\hat{\eta}}{\partial\hat{t}}(\hat{r},0) = 0, \quad \hat{\phi}(\hat{r},\hat{z},0) = 0 \tag{2.6a,b}$$

In (2.6*a*,*b*), l_q belongs to the set of (non-trivial) zeroes of $\mathrm{J}_1(\cdot)$ with $q = 1, 2, 3\ldots$, i.e. $\mathrm{J}_1(l_q) = 0$. This choice ensures that the initial condition satisfies (2.5*a*,*b*). For ease of algebra, we operate on (2.3) by $\mathrm{D}/\mathrm{D}\hat{t}$ replacing $\hat{\eta}$ in the gravity term with derivatives of $\hat{\phi}$ using (2.2) (Penney *et al.* 1952). In further calculations, we replace the kinematic boundary condition (2.2) with this equation. The resulting equations are then written in cylindrical axisymmetric coordinates ((1.1)–(1.6) in accompanying supplementary material available at https://doi.org/10.1017/jfm.2020.851) and non-dimensionalised using

$$r = \frac{l_q\hat{r}}{\hat{R}_0}, \quad z = \frac{l_q\hat{z}}{\hat{R}_0}, \quad t = \left(\frac{gl_q}{\hat{R}_0}\right)^{1/2}\hat{t}, \quad \eta = \frac{l_q\hat{\eta}}{\hat{R}_0} \quad \text{and} \quad \phi = \left(\frac{l_q^3}{g\hat{R}_0^3}\right)^{1/2}\hat{\phi}. \tag{2.7a–e}$$

https://doi.org/10.1017/jfm.2020.851 Published online by Cambridge University Press

This leads to the following set:

$$\frac{\partial^2\phi}{\partial r^2}+\frac{1}{r}\frac{\partial\phi}{\partial r}+\frac{\partial^2\phi}{\partial z^2}=0, \tag{2.8}$$

$$\left(\frac{\partial^2\phi}{\partial t^2}+\frac{\partial\phi}{\partial z}+\left\{\frac{\partial}{\partial t}+\frac{1}{2}\left(\frac{\partial\phi}{\partial r}\right)\frac{\partial}{\partial r}+\frac{1}{2}\left(\frac{\partial\phi}{\partial z}\right)\frac{\partial}{\partial z}\right\}|\nabla\phi|^2\right)_{z=\eta}$$
$$-\sigma\left\{\left[\frac{\partial}{\partial t}+\left(\frac{\partial\phi}{\partial r}\right)_{z=\eta}\frac{\partial}{\partial r}\right]\left(\frac{\dfrac{\partial^2\eta}{\partial r^2}}{\left\{1+\left(\dfrac{\partial\eta}{\partial r}\right)^2\right\}^{3/2}}+\frac{1}{r}\frac{\dfrac{\partial\eta}{\partial r}}{\left\{1+\left(\dfrac{\partial\eta}{\partial r}\right)^2\right\}^{1/2}}\right)\right\}=0, \tag{2.9}$$

$$\left(\frac{\partial\phi}{\partial t}+\frac{1}{2}|\nabla\phi|^2+z\right)_{z=\eta}-\sigma\left(\frac{\dfrac{\partial^2\eta}{\partial r^2}}{\left\{1+\left(\dfrac{\partial\eta}{\partial r}\right)^2\right\}^{3/2}}+\frac{1}{r}\frac{\dfrac{\partial\eta}{\partial r}}{\left\{1+\left(\dfrac{\partial\eta}{\partial r}\right)^2\right\}^{1/2}}\right)=0, \tag{2.10}$$

$$\int_0^{l_q} r\eta(r,t)\,\mathrm{d}r=0, \tag{2.11}$$

$$\left(\frac{\partial\phi}{\partial r}\right)_{r=0}=\left(\frac{\partial\phi}{\partial r}\right)_{r=l_q}=0,\quad \left(\frac{\partial\eta}{\partial r}\right)_{r=0}=\left(\frac{\partial\eta}{\partial r}\right)_{r=l_q}=0, \tag{2.12a,b}$$

$$\text{and}\quad \eta(r,0)=\epsilon\mathrm{J}_0(r),\quad \frac{\partial\eta}{\partial t}(r,0)=0,\quad \phi(r,z,0)=0, \tag{2.13a–c}$$

Equations (2.8)–(2.13*a–c*) contain two non-dimensional groups *viz.* the nonlinearity parameter $\epsilon\equiv a_0(l_q/\hat{R}_0)$ and $\sigma\equiv T(l_q/\hat{R}_0)^2/\rho g$ which measures the relative strength of surface tension to gravity and is the inverse of Bond number. Note that ϵ appears in the initial condition while σ appears in the boundary condition. It is important to remember in further analysis that q is a fixed integer serving as an index for the primary mode. In this study q has been chosen to be 5, to remain consistent with the deep water approximation treated here. We treat ϵ as a small parameter with $\sigma=O(1)$ expanding ϕ, η and t in (2.8)–(2.12*a,b*) as

$$\phi(r,z,t)=0+\epsilon\phi_1(r,z,t)+\epsilon^2\phi_2(r,z,t)+\epsilon^3\phi_3(r,z,t)+O(\epsilon^4), \tag{2.14}$$

$$\eta(r,t)=0+\epsilon\eta_1(r,t)+\epsilon^2\eta_2(r,t)+\epsilon^3\eta_3(r,t)+O(\epsilon^4), \tag{2.15}$$

$$\tau=t\left[1+\epsilon^2\Omega_2+O(\epsilon^3)\right]. \tag{2.16}$$

The expansion of t in (2.16) is a standard Lindstedt–Poincaré technique and is necessary in order to take into account the nonlinear dependence of the oscillation frequency on the amplitude ϵ of the Bessel modes. Substituting (2.14)–(2.16) into (2.8)–(2.13*a–c*) and using Taylor series expansions about $z=0$, we may generically write at any

https://doi.org/10.1017/jfm.2020.851 Published online by Cambridge University Press

$O(\epsilon^i)$ $(i = 1, 2, 3, \ldots)$

$$\frac{\partial^2 \phi_i}{\partial r^2} + \frac{1}{r}\frac{\partial \phi_i}{\partial r} + \frac{\partial^2 \phi_i}{\partial z^2} = 0, \tag{2.17}$$

$$\left(\frac{\partial^2 \phi_i}{\partial \tau^2} + \frac{\partial \phi_i}{\partial z}\right)_{z=0} - \sigma\left[\left(\frac{\partial^3 \eta_i}{\partial \tau \partial r^2}\right) + \frac{1}{r}\left(\frac{\partial^2 \eta_i}{\partial \tau \partial r}\right)\right] = G_i(r, \tau), \tag{2.18}$$

$$\left(\frac{\partial \phi_i}{\partial \tau}\right)_{z=0} + \eta_i - \sigma\left[\left(\frac{\partial^2 \eta_i}{\partial r^2}\right) + \frac{1}{r}\left(\frac{\partial \eta_i}{\partial r}\right)\right] = F_i(r, \tau), \tag{2.19}$$

$$\int_0^{l_q} r\eta_i(r, t)\,\mathrm{d}r = 0, \tag{2.20}$$

$$\left(\frac{\partial \phi_i}{\partial r}\right)_{r=0} = \left(\frac{\partial \phi_i}{\partial r}\right)_{r=l_q} = 0, \quad \left(\frac{\partial \eta_i}{\partial r}\right)_{r=0} = \left(\frac{\partial \eta_i}{\partial r}\right)_{r=l_q} = 0, \tag{2.21a,b}$$

$$\eta_i(r, 0) = \mathrm{J}_0(r)\delta_{1i}, \quad \frac{\partial \eta_i}{\partial \tau}(r, 0) = \phi_i(r, z, 0) = 0, \tag{2.22a,b}$$

where δ_{ij} is the Kronecker delta. As is usual in perturbative methods, the only difference at different orders in (2.18) and (2.19) are the expressions F_i and G_i on the right-hand side. Here $F_1(r, \tau) = G_1(r, \tau) = 0$ while $F_2(r, \tau), G_2(r, \tau), F_3(r, \tau), G_3(r, \tau)$ have lengthy expressions provided in appendix A. Our task is to now solve (2.17)–(2.22*a*,*b*) up to $i = 2$ (second order). Note that for determining the solution up to $i = 2$ completely, it is necessary to also obtain the equations at $i = 3$.

Observe that $\phi(r, z, \tau) = p(\tau)\mathrm{J}_0(\alpha r)\exp[\alpha z]$ satisfies the axisymmetric Laplace equation (2.17) for any (real) α and $p(\tau)$. In addition, if we choose $\eta(r, \tau) = a(\tau)\mathrm{J}_0(l_j(r/l_q))$ and $\phi(r, z, \tau) = p(\tau)\mathrm{J}_0(l_j(r/l_q))\exp(l_j(z/l_q))$, the identity $\int_0^{l_q} \mathrm{J}_0(l_j(r/l_q))\, r\,\mathrm{d}r = 0$ and the equation $\mathrm{J}_1(l_j) = 0\ \forall j \in \mathbb{Z}^+$ ensure that (2.20) and (2.21*a*,*b*) are also satisfied. Thus the general solution for ϕ_i and η_i satisfying (2.17) and conditions (2.20) and (2.21*a*,*b*) may be posed as an eigenfunction expansion (Dini series, Mack 1962)

$$\phi_i(r, z, \tau) = \sum_{j=0}^{\infty} p_i^{(j)}(\tau)\mathrm{J}_0\left(\alpha_j r\right)\exp\left(\alpha_j z\right), \tag{2.23}$$

$$\eta_i(r, \tau) = \sum_{j=0}^{\infty} a_i^{(j)}(\tau)\mathrm{J}_0\left(\alpha_j r\right) \quad \text{with } \alpha_j \equiv \frac{l_j}{l_q}. \tag{2.24}$$

Substituting (2.23) and (2.24) into (2.18) and (2.19) and using orthogonality relations among Bessel functions (see supplementary material), we obtain the following equations governing the coefficients $p_i^m(\tau)$ and $a_i^m(\tau)$ at any order $O(\epsilon^i)$:

$$\frac{\mathrm{d}^2 p_i^{(m)}}{\mathrm{d}\tau^2} + \omega_m^2 p_i^{(j)}(\tau) = \left(1 + \sigma\alpha_m^2\right)\mathbb{G}_i^{(m)}(\tau) - \sigma\alpha_m^2\frac{\mathrm{d}\mathbb{F}_i^{(m)}}{\mathrm{d}\tau}, \tag{2.25}$$

$$a_i^{(m)}(\tau) = \frac{1}{1 + \sigma\alpha_m^2}\left(\mathbb{F}_i^{(m)}(\tau) - \frac{\mathrm{d}p_i^{(m)}}{\mathrm{d}\tau}\right), \quad m = 0, 1, 2\ldots. \tag{2.26}$$

https://doi.org/10.1017/jfm.2020.851 Published online by Cambridge University Press

Here $\omega_m^2 \equiv \alpha_m(1+\sigma\alpha_m^2)$ is the deep-water linear dispersion relation for capillary-gravity waves written in scaled variables. $\mathbb{F}_i^{(m)}(\tau)$ and $\mathbb{G}_i^{(m)}(\tau)$ in (2.25) and (2.26) are defined as

$$\left.\begin{aligned}\mathbb{G}_i^{(m)}(\tau) &\equiv \frac{2}{l_q^2 \mathrm{J}_0^2(l_m)}\int_0^{l_q} \mathrm{d}r r \mathrm{J}_0(\alpha_m r)\, G_i(r,\tau),\\ \mathbb{F}_i^{(m)}(\tau) &\equiv \frac{2}{l_q^2 \mathrm{J}_0^2(l_m)}\int_0^{l_q} \mathrm{d}r r \mathrm{J}_0(\alpha_m r)\, F_i(r,\tau).\end{aligned}\right\} \tag{2.27}$$

Equation (2.25) may now be solved for $p_i^{(m)}(\tau)$ (with suitable initial conditions) and the resultant solution determines $a_i^{(m)}(\tau)$ using (2.26). With $m = 0, 1, 2, 3\ldots$ and $i = 1, 2, 3\ldots$, the initial conditions from (2.22*a*,*b*) are

$$p_i^{(m)}(0) = 0, \quad \frac{\mathrm{d}p_i{}^{(m)}}{\mathrm{d}\tau}(0) = \mathbb{F}_i^{(m)}(0) - \left(1+\sigma\alpha_m^2\right)\delta_{mq}\delta_{i1}, \tag{2.28a,b}$$

$$a_i^{(m)}(0) = \delta_{mq}\delta_{i1}, \quad \frac{\mathrm{d}a_i^{(m)}}{\mathrm{d}\tau}(0) = 0. \tag{2.29a,b}$$

We determine $p_i^m(\tau)$ and $a_i^m(\tau)$ using (2.25) and (2.26), respectively, at various orders using initial conditions (2.28*a*,*b*) and (2.29*a*,*b*).

2.2. *Linear solution: $O(\epsilon)$*

At $O(\epsilon)$, the solution is elementary. It is shown in the accompanying supplementary material that at linear order, the only non-zero term in the eigenfunction expansion in (2.23) and (2.24) is for $j = q$, the primary mode. With $\omega_q^2 = 1+\sigma$, this leads to,

$$\phi_1(r,z,\tau) = -\omega_q \sin(\omega_q\tau)\mathrm{J}_0(r)\exp(z), \quad \eta_1(r,\tau) = \cos(\omega_q\tau)\mathrm{J}_0(r). \tag{2.30a,b}$$

2.3. *Nonlinear corrections: $O(\epsilon^2)$*

At $O(\epsilon^2)$, the calculation is algebraically tedious and quite lengthy, but otherwise standard. We outline the key results below, referring the interested reader to the accompanying supplementary material for the detailed derivation. Using (2.23) and (2.24), we obtain at $O(\epsilon^2)$,

$$\eta_2(r,\tau) = \sum_{k=1}^{\infty}\left[\zeta_1^{(k)}\cos(\omega_k\tau) + \zeta_2^{(k)}\cos(2\omega_q\tau) + \zeta_3^{(k)}\right]\mathrm{J}_0(\alpha_k r), \tag{2.31}$$

$$\phi_2(r,z,\tau) = \frac{\mathrm{J}_0^2(l_q)}{2}\sin\left(2\omega_q\tau\right) + \sqrt{1+\sigma}\sum_{k=1}^{\infty}\left[\xi_1^{(k)}\sin(\omega_k\tau) + \xi_2^{(k)}\sin\left(2\omega_q\tau\right)\right]\mathrm{J}_0(\alpha_k r)\exp(\alpha_k z), \tag{2.32}$$

where expressions for $\zeta_1^{(k)}, \zeta_2^{(k)}, \zeta_3^{(k)}$ and $\xi_1^{(k)}, \xi_2^{(k)}$ are provided in appendix B. Note the presence of terms in (2.31) and (2.32), which are pure functions of space and time, respectively. This implies that there is a nonlinear correction to the (temporal) mean interface level, note the third term in (2.31) whose time average is non-zero.

https://doi.org/10.1017/jfm.2020.851 Published online by Cambridge University Press

Similarly there is a nonlinear correction in ϕ whose spatial average is non-zero. An important thing to note in the nonlinear solution (2.31) and (2.32) is the presence of the entire spectrum (and not just the qth primary mode) at this order, which implies a nonlinear transfer of energy to the entire spectrum. This transfer of energy will be seen to be crucial to jetting.

Despite having expressions for $\phi(r, z, \tau)$ and $\eta(r, \tau)$ up to $O(\epsilon^2)$, our calculation is incomplete, as a nonlinear correction to the dispersion relation $\omega_m^2 = \alpha_m(1 + \alpha_m^2\sigma)$ $[1 + O(\epsilon^2)]$ is expected at this order, through Ω_2 in (2.16). For determining this, it is necessary to proceed to the third order ($O(\epsilon^3)$) where elimination of resonant forcing of the primary mode (subscript q) will determine this correction. We emphasise that we do not determine the $O(\epsilon^3)$ corrections to $\phi(r, z, \tau)$ and $\eta(r, \tau)$. A minimal $O(\epsilon^3)$ calculation is carried out for determining Ω_2. This is done by obtaining the equations governing $p_3^{(m)}(\tau)$ and setting the coefficient of the resonant forcing term (for the primary mode) to zero. In this way, we obtain after some lengthy algebraic manipulations (see supplementary material)

$$\begin{aligned}\Omega_2 = \frac{1}{2\mathrm{J}_0^2(l_q)}\Bigg[\sum_{l=1}^{\infty}\Big[\Big\{\big[\alpha_l(2+\sigma)-\alpha_l^2\big]\xi_2^{(l)}+2\sigma\zeta_2^{(l)}\Big\}I_{0-l,0-q,0-q} \\ -\Big\{2(1+\sigma)\alpha_l\xi_2^{(l)}+\alpha_l^3\sigma\zeta_2^{(l)}-2\alpha_l^3\sigma\zeta_3^{(l)}\Big\}I_{0-q,1-q,1-l}\Big] \\ -\frac{(1+\sigma)}{2}I_{0-q,0-q,0-q,0-q}+\frac{\left(1-4\sigma+\sigma^2\right)}{4(1+\sigma)}I_{0-q,0-q,1-q,1-q} \\ +\frac{3\left(1+3\sigma+\sigma^2\right)}{4(1+\sigma)}I_{0-q,1-q,1-q,2-q}\Bigg].\end{aligned} \tag{2.33}$$

Note that as shorthand notation in (2.33) we have used

$$I_{\nu_1-m_1,\nu_2-m_2,\ldots} \equiv \int_0^1 \mathrm{d}\tilde{r}\,\tilde{r}\,\mathrm{J}_{\nu_1}\left(l_{m_1}\tilde{r}\right)\mathrm{J}_{\nu_2}\left(l_{m_2}\tilde{r}\right)\ldots \tag{2.34}$$

where $\tilde{r} \equiv r/l_q$ and $\nu_i, m_i = 0, 1, 2, \ldots$, e.g.

$$I_{0-m,1-q,1-q} \equiv \int_0^1 \mathrm{d}\tilde{r}\,\tilde{r}\,\mathrm{J}_0\left(l_m\tilde{r}\right)\mathrm{J}_1^2\left(l_q\tilde{r}\right). \tag{2.35}$$

With $\sigma = 1.086$ and parameters corresponding to air–water (see table 3), the amplitude correction to the dispersion relation for the primary mode $q = 5$ evaluates to $\Omega_2 \approx -0.0332$, using expression (2.33).

2.4. *Summary of weakly nonlinear theory*

We may now combine results up to $O(\epsilon^2)$ to predict

$$\begin{aligned}\eta(r,\tau) = \epsilon\mathrm{J}_0(r)\cos\left(\omega_q\tau\right)+\epsilon^2\sum_{k=1}^{\infty}\left[\zeta_1^{(k)}\cos\left(\omega_k\tau\right)+\zeta_2^{(k)}\cos\left(2\omega_q\tau\right)+\zeta_3^{(k)}\right]\mathrm{J}_0\left(\alpha_k r\right) \\ +O(\epsilon^3),\end{aligned} \tag{2.36}$$

https://doi.org/10.1017/jfm.2020.851 Published online by Cambridge University Press

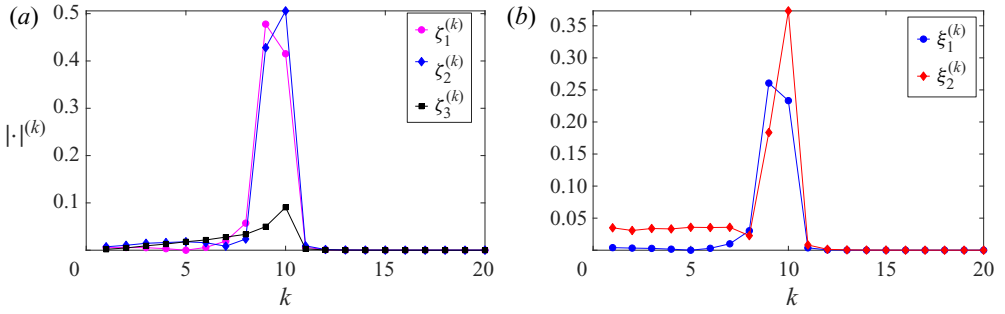

FIGURE 4. Here, $\zeta_1^{(k)}$, $\zeta_2^{(k)}$, $\zeta_3^{(k)}$ and $\xi_1^{(k)}$, $\xi_2^{(k)}$ for $q = 5$ as a function of k. After $k = 12$, the values are quite small permitting truncation of the infinite series in (2.36) and (2.37).

$$\phi(r, z, \tau) = -\epsilon\omega_q \mathrm{J}_0(r) \exp(z) \sin\left(\omega_q \tau\right) + \epsilon^2 \frac{\mathrm{J}_0^2(l_q)}{2} \sin\left(2\omega_q \tau\right) + \epsilon^2 \sqrt{1+\sigma} \sum_{k=1}^{\infty} \left[\xi_1^{(k)} \sin\left(\omega_k \tau\right) + \xi_2^{(k)} \sin\left(2\omega_q \tau\right)\right] \mathrm{J}_0\left(\alpha_k r\right) \exp\left(\alpha_k z\right) + O(\epsilon^3) \tag{2.37}$$

$$\text{and} \quad \omega_k^2 = \alpha_k \left(1 + \sigma\alpha_k^2\right) \left[1 + \epsilon^2 \Omega_2 + O(\epsilon^3)\right], \tag{2.38}$$

where Ω_2 is given by (2.33). It may be checked that (2.36) and (2.37) satisfy the initial conditions (2.13*a–c*). In particular $\zeta_1^{(k)} + \zeta_2^{(k)} + \zeta_3^{(k)} = 0$ for all $k = 1, 2 \ldots$ which ensures that $\eta(r, 0) = \epsilon \mathrm{J}_0(r)$. Other initial conditions in (2.13*a–c*) involving the time derivative of $\eta(r, t)$ and on $\phi(r, z, 0)$ are trivially verified. The singularity of the expressions for $\xi_1^{(k)}$, $\xi_2^{(k)}$, etc. at a possible $\omega_k = 2\omega_q$ is discussed further in § 6. As (2.36) and (2.37) are an infinite series, we truncate them for numerical evaluation in later sections. For any r, z and τ, it may be expected that the infinite sums in (2.36) and (2.37) have progressively smaller contributions at higher values of k. This is seen in figures 4(*a*) and 4(*b*) where we have evaluated the coefficients $\zeta_1^{(k)}$, $\zeta_2^{(k)}$, $\zeta_3^{(k)}$ and $\xi_1^{(k)}$, $\xi_2^{(k)}$ for the primary mode $q = 5$ as a function of k in (2.36) and (2.37). It is seen that the peak values are at around $k = 10$ which is expected, as this is the second multiple of $q = 5$ and our calculation is accurate up to $O(\epsilon^2)$. Thus for $q = 5$, one needs to retain at least 10 terms while numerically evaluating the infinite series (2.36) and (2.37). For high accuracy, we have retained the first 85 terms in our expansions. All the integrals that appear in $\zeta_1^{(k)}$, $\zeta_2^{(k)} \ldots$ have been evaluated numerically using MATLAB (MAT 2018).

3. Numerical simulations

In this section, we provide a brief description of the code used for numerical simulations of the incompressible Euler equation with surface tension supplemented with an equation for tracking the interface, *viz.* (3.1*a*,*b*) and (3.2). The simulations have been performed using the open-source code Basilisk (Popinet 2020), a successor to the well-known open-source solver Gerris (Popinet 2003, 2009). These codes have been carefully benchmarked on a suite of interfacial flow problems over many years and results using these have extensively appeared in the literature, e.g. Agbaglah *et al.* (2011), Dasgupta, Tomar & Govindarajan (2015), Farsoiya *et al.* (2017), Fuster & Popinet (2018), Deike *et al.* (2018), Lai *et al.* (2018), Singh, Farsoiya & Dasgupta (2019),

https://doi.org/10.1017/jfm.2020.851 Published online by Cambridge University Press

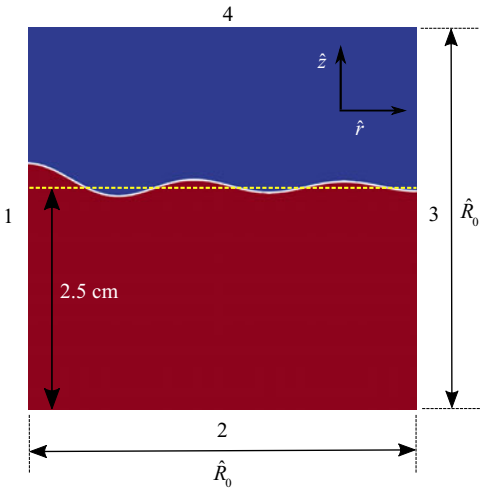

FIGURE 5. Initial condition.

Blanco-Rodríguez & Gordillo (2020) and Dhar, Das & Das (2020), to mention only a small set. Basilisk implements the finite-volume algorithm using the Bell–Collela–Glaz (Bell, Colella & Glaz 1989) advection scheme. A semi-implicit scheme is utilised to calculate velocity and pressure fields. For capturing the interface, the geometric volume of fluid method (Scardovelli & Zaleski 1999) is used along with the continuum surface force model for including surface tension as a body force into the momentum equations (Brackbill, Kothe & Zemach 1992; Popinet 2018). An important point to note in the context of the present study is that Basilisk implements the one-fluid model, and hence necessarily solves for both air and water. In contrast, the weakly nonlinear analysis described earlier ignores the inertial effect of air, assuming it to be a relatively low density gas compared with water. Thus, when comparing our numerical simulations, minor differences are expected between theory and simulations near the interface;

$$\nabla \cdot \boldsymbol{u} = 0, \quad \frac{\partial \boldsymbol{u}}{\partial t} + \nabla \cdot (\boldsymbol{u} \otimes \boldsymbol{u}) = -\frac{1}{\rho}\nabla p + \boldsymbol{g} + \frac{T}{\rho}\kappa \delta_s \boldsymbol{n}, \tag{3.1a,b}$$

$$\frac{\partial f}{\partial t} + \nabla \cdot (f\boldsymbol{u}) = 0. \tag{3.2}$$

In (3.1*a*,*b*) and (3.2), $\boldsymbol{u}$, p, T, κ and f are velocity, pressure, surface tension coefficient, curvature and volume fraction fields, respectively. The computational box is depicted in figure 5 with boundary conditions in table 2. Note that boundary #1 in figure 5 is the axis of symmetry. Parameters for the simulations are reported in table 3. Case 9 in table 3 represent a set of numerical simulations used for scaling analysis. The parameters for these are numerous and listed in the accompanying supplementary material. Note that some of the simulations for this case deviate from air–water parameters with respect to surface tension. The density of air (in the centimetre–gram–second system of units) has been chosen to be 0.001. Simulations are done with uniform 1024×1024 and 2048×2048 grids and are tested for convergence, with grid refinement (see accompanying supplementary material). A repository with script files has been set up in Basak, Farsoiya

https://doi.org/10.1017/jfm.2020.851 Published online by Cambridge University Press

Boundary	Velocity ($\hat{\boldsymbol{u}}$)		Pressure ($\hat{P}$)	f
#	$\hat{u}_r$	$\hat{u}_z$		
1	D	N	N	N
2	N	D	N	N
3	D	N	N	N
4	N	D	N	N

D: Dirichlet N: Neumann

TABLE 2. Boundary conditions.

Case	Grid	a_0	ρ	T	$\hat{R}_0$	$l_q(q=5)$	$\sigma \equiv \frac{T(l_q/\hat{R}_0)^2}{\rho g}$	$\epsilon \equiv \frac{a_0 l_q}{\hat{R}_0}$
0	(a)	0.052	1.0	72	4.282	16.4706	1.086	0.2
1	(a),(b)	0.130	”	”	”	”	”	0.5
2	(a)	0.208	”	”	”	”	”	0.8
3	(a)	0.260	”	”	”	”	”	1.0
4	(a)	0.286	”	”	”	”	”	1.1
5	(a),(b)	0.312	”	”	”	”	”	1.2
6	(a)	0.338	”	”	”	”	”	1.3
7	(a)	0.364	”	”	”	”	”	1.4
8	(a),(b)	0.442	”	”	”	”	”	1.7
9	(a)	$\{a_{0i}\}$	”	$\{T_i\}$	”	”	$\{\sigma_i\}$	$\{\epsilon_i\}$

TABLE 3. Simulation parameters in the centimetre–gram–second system of units. Grid (a) 1024×1024; grid (b) 2048×2048.

& Dasgupta (2020), using which the results discussed below may be reproduced. The Basilisk script file is also provided as additional supplementary material.

4. Results and analysis

We test theoretical predictions against numerical simulations here and provide detailed comparisons and analysis in the following subsections.

4.1. *Tracking the interface at $r = 0$*

In figure 6, we show the time signals obtained by tracking the interface at $r = 0$. For $\epsilon = 0.2$ in figure 6(a) a very good match is seen with the linearised theoretical predictions. Already at $\epsilon = 0.5$ (figure 6b), visible differences appear with the linearised prediction. The insets in all panels in figure 6 depict the instantaneous shape of the interface at the time instant indicated by the arrow. In figures 6(c) and 6(d) we have plotted the signals for $\epsilon = 1.2$ and $\epsilon = 1.7$, respectively. While the agreement with theory is moderately good in figure 6(c), the linearised signal clearly shows a poor match. In figure 6(d), where $\epsilon = 1.7$, a slender jet is produced in numerical simulations ejecting a drop from its tip. Here the nonlinear theory significantly improves over the linear prediction but produces a somewhat broader jet without the droplet ejection at the tip, see inset. As seen in figures 6(c) and 6(d), at the end of one oscillation the height of the (scaled) interface

https://doi.org/10.1017/jfm.2020.851 Published online by Cambridge University Press

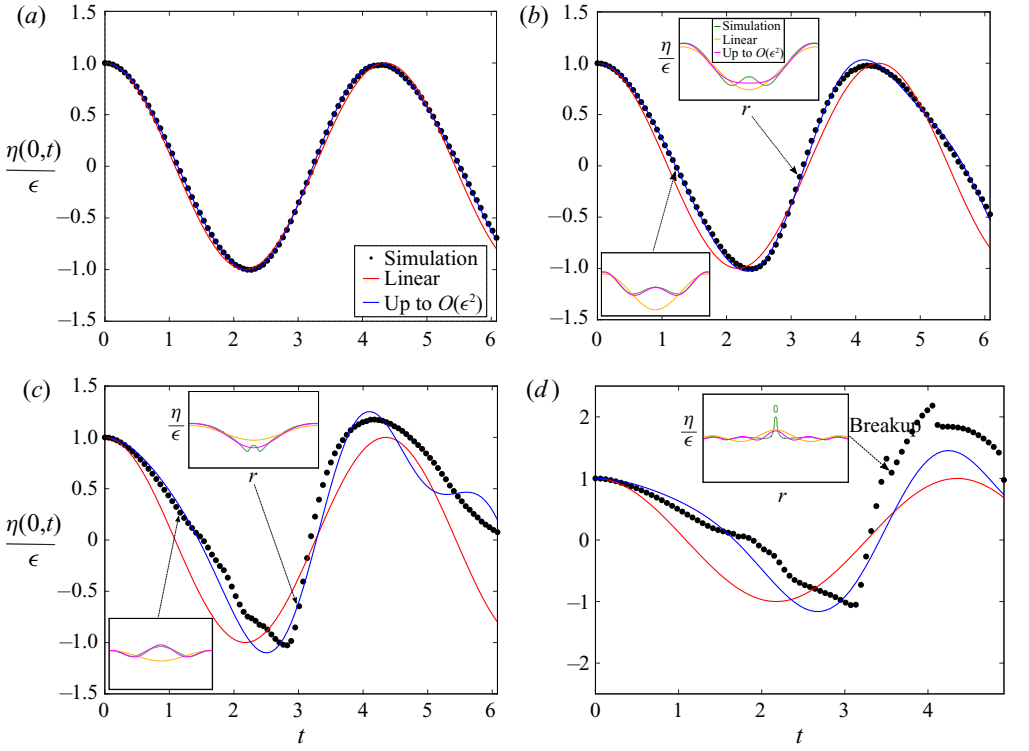

FIGURE 6. Motion of the interface at $r = 0$ with time t: (*a*) $\epsilon = 0.2 \ll 1$, no jetting in linear regime; (*b*) at moderately large $\epsilon = 0.5$ interface shows dimple formation, see insets depicting instantaneous interface shape (η/ϵ versus r) at the data point indicated by arrow. Weakly nonlinear model captures the onset of dimple at $t \approx 1.228$ but does not describe it well later at $t \approx 3.133$ when it narrows and sharpens. Pronounced dimple and a clear overshoot (above unity) is observed in panel (*c*) for $\epsilon = 1.2$. (*d*) For $\epsilon = 1.7$, a slender jet with large overshoot and droplet ejection at the tip. While weakly nonlinear theory captures the qualitative features, linear theory is unable to describe any of these.

at $r = 0$ is significantly more than unity. This overshoot is a signature of jetting which the nonlinear theory manages to capture reasonably well. Another interesting feature seen in the upper insets of figures 6(*b*) and 6(*c*) is the appearance of a small dimple which is a known precursor to jet formation in other scenarios such as bubble bursting (Deike *et al.* 2018; Gañán-Calvo 2017). Note that this dimple already starts appearing as a broader structure during the earlier downward motion of the cavity and at that instant is well described by the nonlinear theory (bottom insets in figures 6*b* and 6*c*). This, however, gets smoothed out as the cavity reaches its lower extremity. Note that the abrupt drop in amplitude around $t \approx 3.8$ in figure 6(*d*) is due to ejection of a droplet. A point worth noting here is that for $\epsilon = 1.2$, we see that the $O(\epsilon^2)$ predictions work reasonably well (figure 6*c*) despite the fact that the theory is strictly valid only for $\epsilon < 1$. This is a recurrent situation in fluid dynamical problems involving a small parameter, e.g. in boundary layer theory the parallel flow assumption involves errors at least of $O(Re^{-1/3})$ (Govindarajan & Narasimha 1999; Govindarajan 2004). However, despite this it provides very good predictions for instability down to $Re < 10$, although the magnitude of the error is nearly an order-one number at these Re.

https://doi.org/10.1017/jfm.2020.851 Published online by Cambridge University Press

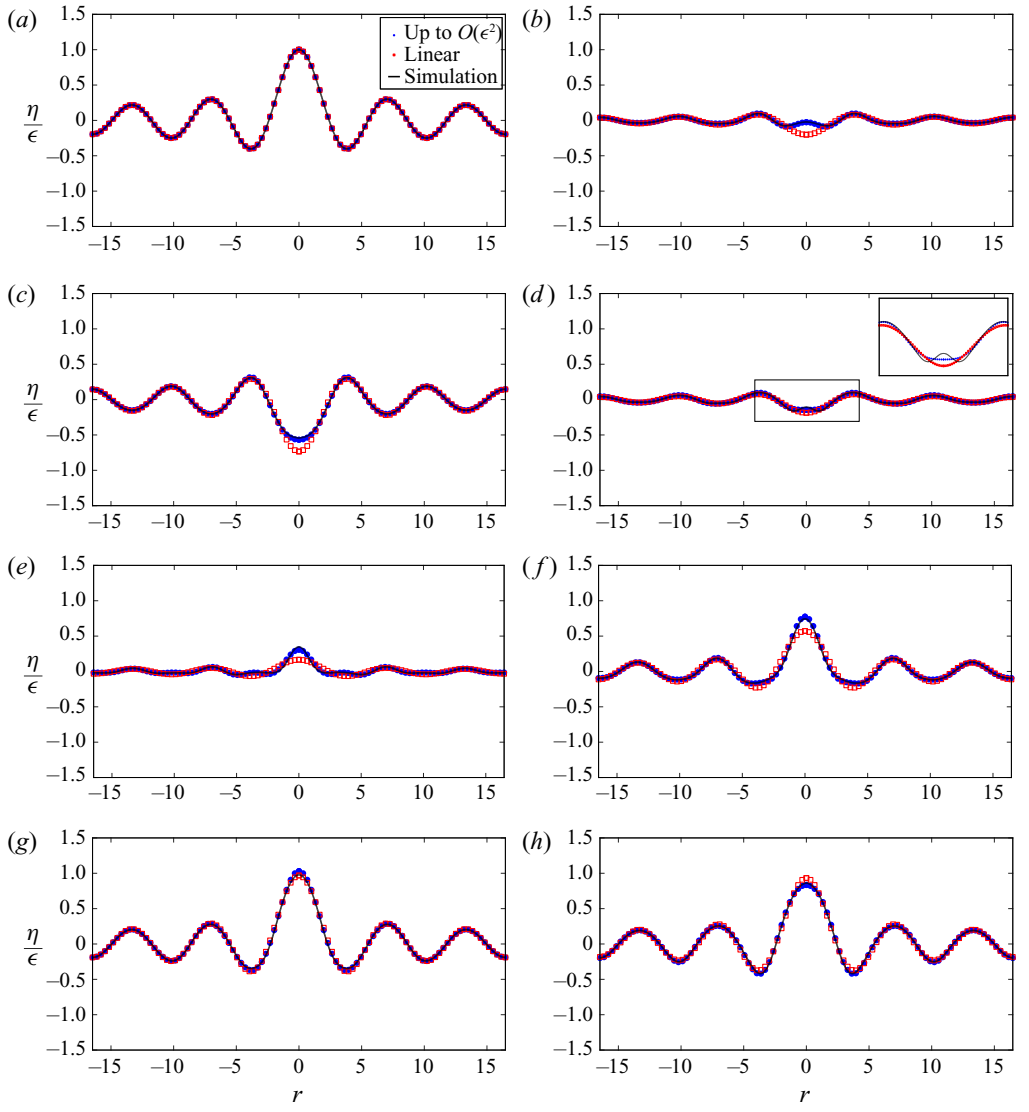

FIGURE 7. (*a–h*) Comparison of the (non-dimensional) interface shape η/ϵ versus radius r at various (non-dimensional) time instants for $\epsilon = 0.5$: (*a*) $t = 0$; (*b*) $t = 1.228$; (*c*) $t = 1.658$; (*d*) $t = 3.133$; (*e*) $t = 3.378$; (*f*) $t = 3.685$; (*g*) $t = 4.177$; (*h*) $t = 4.607$. Simulation profiles (—, black), linear theory (□, red) and weakly nonlinear theory (•, blue). Dimple formation initiates in panel (*b*), is suppressed as the trough reaches its lowest point and reappears with significant shortening in scale as seen in inset of panel (*d*). Weakly nonlinear model qualitatively and significantly improves over the linearised model in this regime. For parameters, see case 1 in table 3, grid (a).

4.2. *Comparison of interface shape*

Comparisons of the interface shape as a function of time are provided in figures 7 and 8 for $\epsilon = 0.5$ and $\epsilon = 1.2$, respectively. Significant nonlinear effects are manifested for a moderately large $\epsilon = 0.5$ in figure 7. In figure 7(*b*), it is seen that at the instant when

https://doi.org/10.1017/jfm.2020.851 Published online by Cambridge University Press

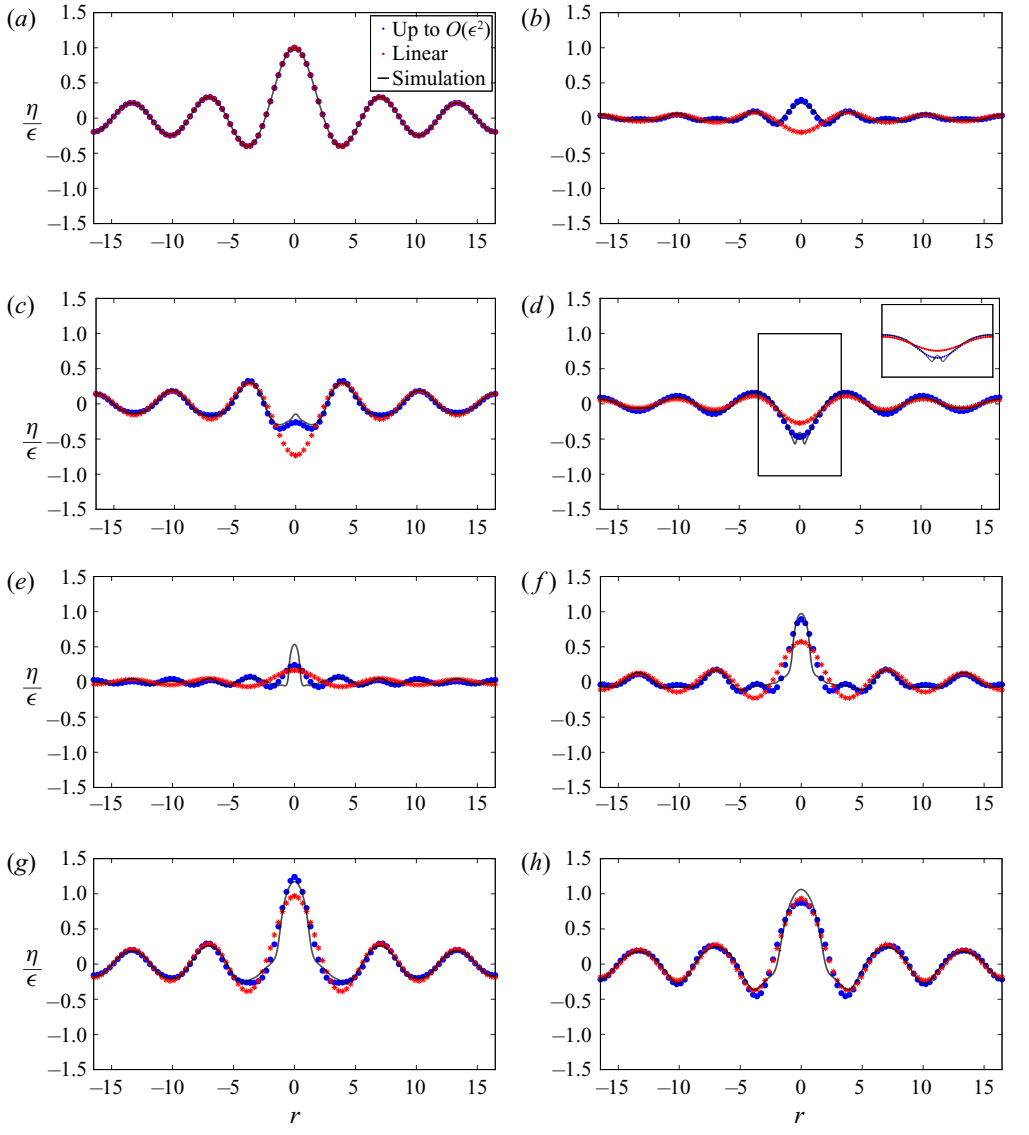

FIGURE 8. (*a–h*) Comparison of the (non-dimensional) interface shape η/ϵ versus radius r at various (non-dimensional) time instants for $\epsilon = 1.2$: (*a*) $t = 0$; (*b*) $t = 1.228$ s; (*c*) $t = 1.658$; (*d*) $t = 3.071$; (*e*) $t = 3.378$; (*f*) $t = 3.685$; (*g*) $t = 4.177$; (*h*) $t = 4.607$. Simulation profiles (—, black) are compared with linear (□, red) and weakly nonlinear predictions (•, blue). Dimple initiation is well captured by the nonlinear theory in panel (*c*) but not later on in panel (*d*) where the dimple becomes sharper and more pronounced, see inset. The thinning of the neck of the jet is not captured by the nonlinear model in panel (*e*). Near maximum overshoot, the jet shape near $r = 0$ is well described by theory, see panel (*f*,*g*). For parameters see case 5 in table 3, grid (b).

dimple formation commences, linear theory makes a large error near $r = 0$, while a good match is seen with the weakly nonlinear theory. As the dimple shrinks in horizontal extent during the upward motion of the cavity in figure 7(*d*), the nonlinear theory captures the interface shape but does not capture the dimple. In the next few snapshots in figure 7(*e–h*),

https://doi.org/10.1017/jfm.2020.851 Published online by Cambridge University Press

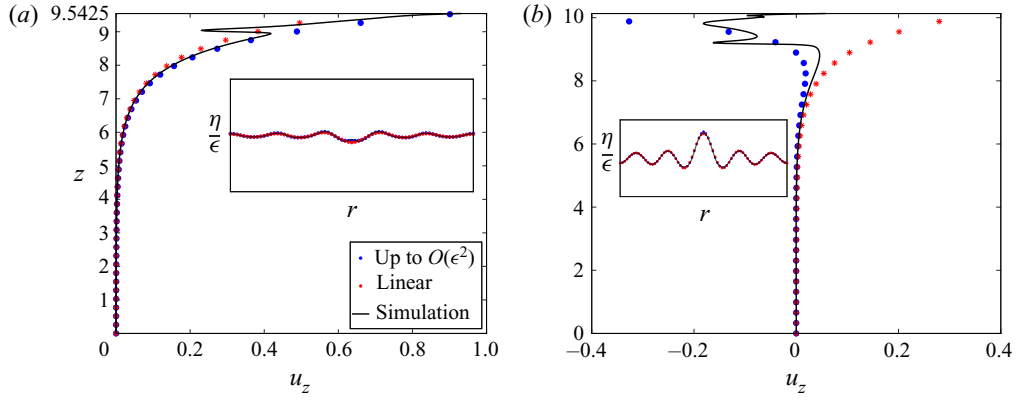

FIGURE 9. Comparison of (non-dimensional) vertical component of velocity u_z at the axis of symmetry ($r = 0$) for $\epsilon = 0.5$ at two time instants: (*a*) $\epsilon = 0.5, t = 3.133$; (*b*) $\epsilon = 0.5, t = 4.177$. Insets show the instantaneous interface shapes. (*a*) Vertical velocity profile when a pronounced dimple forms at the bottom of the trough. (*b*) Velocity profile around the time instant when the interface is at its maximum height. Note the qualitatively good agreement between the weakly nonlinear model and simulations in both cases, although the kinks in the profile are not captured by the nonlinear model. For parameters, see case 1 in table 3, grid (a).

the nonlinear theory captures the time evolution accurately. Similarly for $\epsilon = 1.2$ in figure 8, strong nonlinear effects are visible around $r = 0$ in figure 8(*b*), and particularly in figure 8(*c*) as dimple formation commences. Here weakly nonlinear theory provides an accurate description. However, like in figure 7, the pronounced dimple and its time evolution involving thinning of the jet neck, are not well resolved by the nonlinear prediction as seen in figures 8(*d*) and 8(*e*). Interestingly, the nonlinear theory describes the shape well later in figure 8(*g*), capturing the extent of overshoot (over unity) at $r = 0$ quite well. An important feature is that as ϵ is increased from 0.5 to 1.7 (comparison for $\epsilon = 1.7$ is provided in the supplementary material), the width of the dimple decreases (see insets in figures 7*d* and 8*d*), while the speed at which the tip of the dimple rises upwards increases with increasing ϵ. This may be inferred from the slope of the ascending part of the curve in figures 6(*c*) and 6(*d*).

4.3. *Comparison of vertical velocity and pressure profiles*

Comparisons of the vertical velocity profile at two instants of time are provided in figures 9(*a*) and 9(*b*). It is seen from figure 9(*a*) which corresponds to the pronounced dimple event, that a large vertical velocity develops at the base of the interface. An order-of-magnitude estimate of this velocity maybe obtained using the width of the dimple using the capillary velocity scale (Gordillo & Rodríguez-Rodríguez 2019) $\sqrt{T/\rho W_{dimple}}$, where $W_{dimple} = 0.42$ cm is the dimple width. This yields a (scaled) capillary velocity estimate of around 0.814 in good agreement with the maximum velocity seen in numerical simulations in figure 9(*a*). A good match of the velocity profile with nonlinear theory is seen in figure 9(*a*). Close to the instant of maximum interface height in figure 9(*b*), the velocity profile is almost zero everywhere except in a small region below the interface. In this region, the nonlinear theory predicts the qualitative profile correctly including the negative sign, although some details near the surface are not captured accurately. Note that linear theory predicts an incorrect sign, at this instant.

https://doi.org/10.1017/jfm.2020.851 Published online by Cambridge University Press

In figure 10, we show non-dimensional perturbation pressure profile $P(r, z, t)$ at the axis of symmetry $r = 0$ at various instants for $\epsilon = 0.5$ (and $\epsilon = 1.2$ in the supplementary material). The perturbation pressure field is calculated using $P(r, z, t) = -\partial\phi/\partial t - 1/2|\nabla\phi|^2$. The panels on the right-hand side in figure 10 are perturbation pressure contours from numerical simulations, and the insets show the instantaneous shape of the interface. The plots on the left-hand side show the pressure profile at $r = 0$ as a function of the vertical coordinate z. It is seen clearly from these figures that the formation of the dimple is associated with a region of high positive pressure. When the weakly nonlinear theory is able to capture the onset of the dimple ($t = 1.228$), the agreement between simulations and theory is very good, as verified from figure 10(*a*). However, at $t = 3.133$ when the dimple shrinks in horizontal extent during the upward motion of the cavity, weakly nonlinear theory does not describe the dimple shape accurately and differences are seen between nonlinear theory and simulations especially close to the interface where an incorrect sign of pressure is predicted. It should be noted that an arbitrary shift has been carried out on the pressure data obtained from numerical simulations. This does not affect the conclusions as in the incompressible limit, only gradients of pressure are important.

4.4. *Jet overshoot analysis*

In figure 11, we depict the interface towards the end of one oscillation. Only cases with larger values of ϵ are shown, as in this regime the overshoot of the interface at $r = 0$ above unity is pronounced with the maximum overshoot even exceeding 50 % (figure 11*e*). While the linear theory clearly does not have any overshoot, it is seen that nonlinear theory predicts an overshoot, albeit with varying accuracy. The extent of overshoot depends not only on ϵ but also on σ. This dependence is captured in figure 12 which plots the overshoot ($\hat{a}_{max} \equiv \hat{\eta}(0, t_{max})$) at the end of one oscillation as a function of ϵ at different values of σ. The extent of overshoot is seen to be a strong function of σ as one may intuitively expect. This is because the emergence of the jet involves development of large curvature at the base (pronounced dimple). Surface tension has an opposing effect on this process, and thus for a given ϵ we expect that decreasing surface tension (decreasing σ) promotes jetting and thus overshoot. For moderate to large ϵ, we have fitted the simulation data to an exponential profile of the form $\hat{a}_{max}/a_0 = 1 + A(\sigma)\exp[B(\sigma)\epsilon]$ with $A(\sigma) \ll 1$. Note that for all σ, some data points numerically very close to unity have been removed as these cause $\ln[\hat{a}_{max}/a_0 - 1]$ to be undefined. The inset shows a reasonably good match to a straight line $y = x$ on a semi-log scale. The subplots on the right-hand side of figure 12 show the dependence of $A(\sigma)$ and $B(\sigma)$ on σ. Due to clustering of singularities in σ in the analytical model (see discussion in § 6) in the range $0.02 \leq \sigma \leq 0.6$, it is not possible to compare analytical predictions of overshoot with simulation data in figure 12. To obtain this comparison, we choose σ far away from these singularities *viz.* $\sigma = 1.086$, consistent with our perturbation analysis which assumes that $\sigma = O(1)$. A comparison of the overshoot at the end of one oscillation predicted by the nonlinear expression (2.36) against simulation data is shown in figure 13(*a*). It is seen that there is approximately an 8 %–10 % difference in the extent of overshoot predicted by (2.36) to that seen in simulations, with the former overpredicting the extent of overshoot up to $\epsilon < 1.3$. In figure 13(*b*), we obtain the boundary demarcating the regime where $<10\,\%$ overshoot is observed in our simulations. Here too it is seen that increasing σ requires one to go to increasingly higher values of ϵ in order to obtain overshoot and subsequent jetting.

https://doi.org/10.1017/jfm.2020.851 Published online by Cambridge University Press

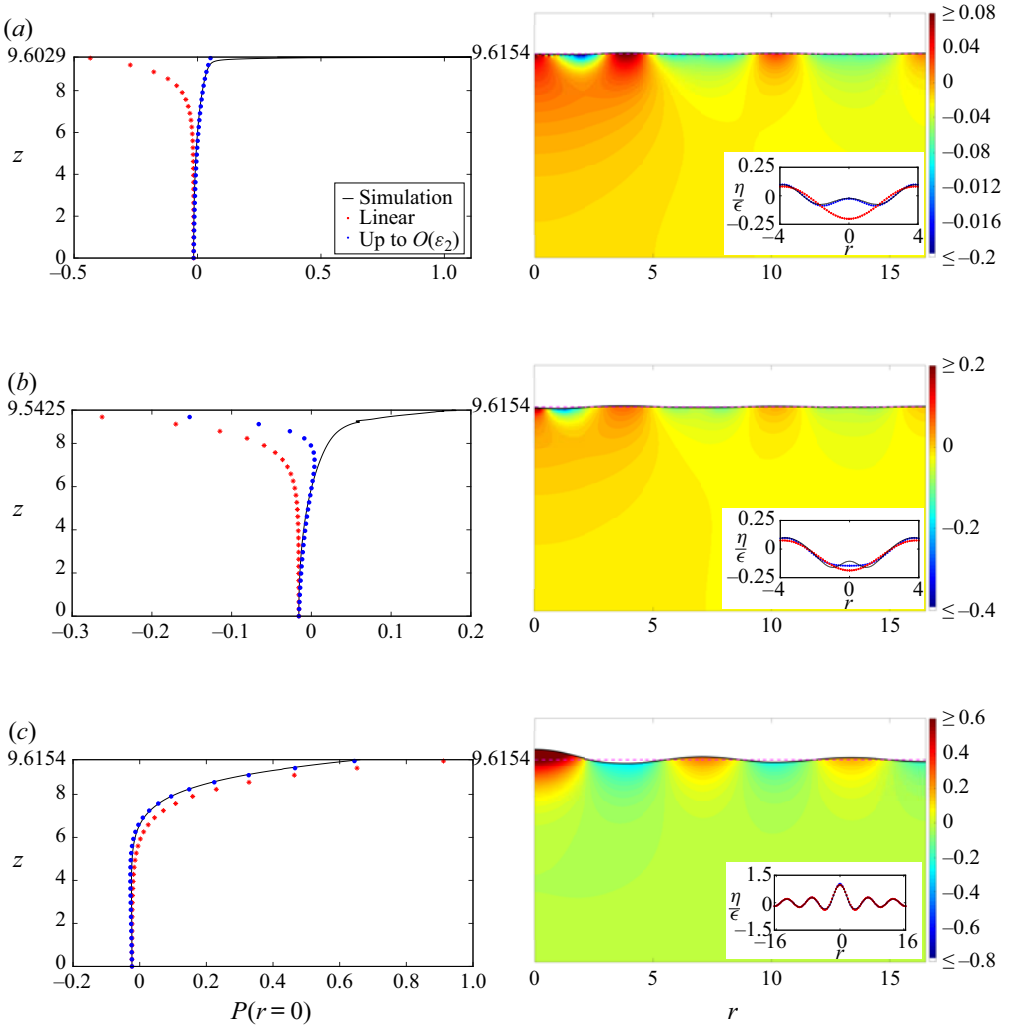

FIGURE 10. Left panels: (non-dimensional) pressure profiles $P(r, z, t)$ at the axis of symmetry $r = 0$ at various time instants for $\epsilon = 0.5$. Right panels: pressure contours from numerical simulations. The dashed line on the contour plots represents the depth of the unperturbed liquid at $t = 0$. The insets depict the instantaneous interface shape. As the weakly nonlinear theory has been derived using a Taylor series expansion about the unperturbed state for the liquid side only, we plot data at most up to the (scaled) unperturbed depth ($z = 9.6154$). For parameters, see case 1 in table 3, grid (a). (*a*) Time $t = 1.228$; pressure profiles (left) and contours (right) at the onset of dimple formation. (*b*) Time $t = 3.133$; pressure profiles and contours with a sharper and narrower dimple. (*c*) Time $t = 4.177$; pressure profiles and contours when the jet is close to its maximum height.

5. Energy and modal analysis

For our system, the total energy is a conserved quantity. Due to truncation of higher-order terms, the weakly nonlinear approximation does not conserve energy exactly and the fluctuations are quantified here. As shown in Zakharov (1968) and Segur & Stewart (2020), the depth averaged total energy per unit horizontal surface area $\rho\hat{E}_{tot}(\hat{r}, \hat{t})$, is

https://doi.org/10.1017/jfm.2020.851 Published online by Cambridge University Press

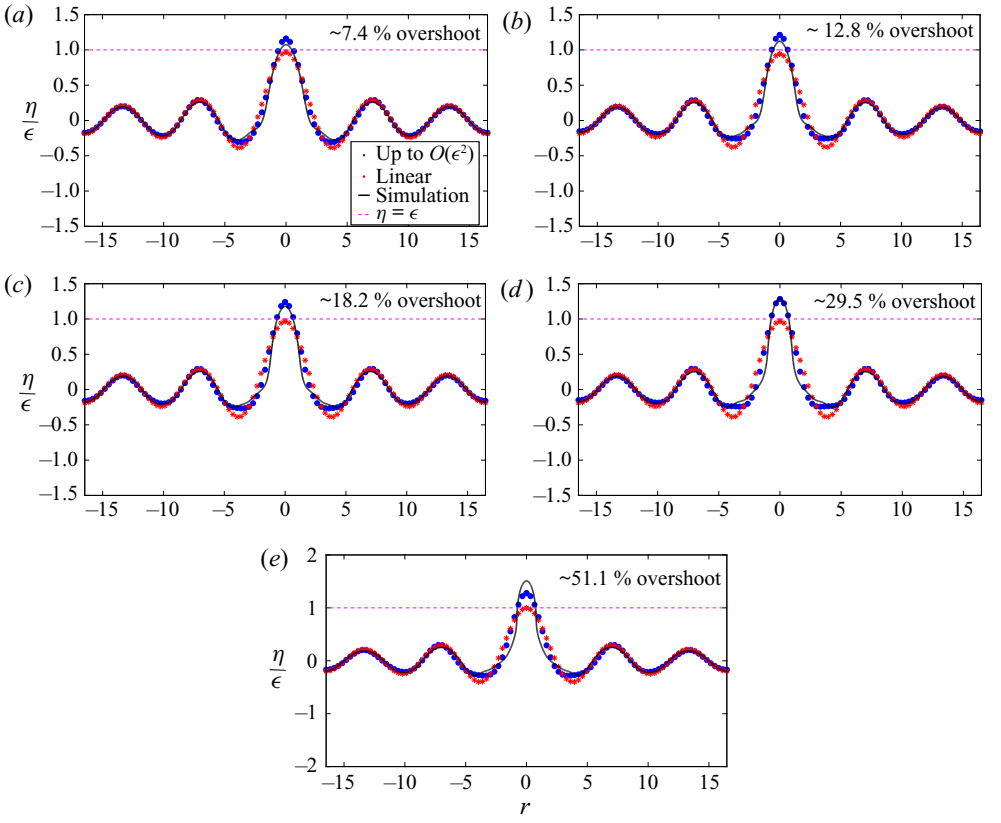

FIGURE 11. The interface shape when the jet is at its maximum height towards the end of one oscillation, for various values of ϵ: (*a*) $\epsilon = 1.0, t = 4.177$; (*b*) $\epsilon = 1.1, t = 4.115$; (*c*) $\epsilon = 1.2, t = 4.177$; (*d*) $\epsilon = 1.3, t = 4.177$; (*e*) $\epsilon = 1.4, t = 4.3$. Overshoot occurs when the scaled interface $\eta(r, t)/\epsilon$ exceeds unity and is always observed at $r = 0$, the axis of symmetry. In the above figures, we show only the ϵ range where a sizeable overshoot (ranging from 7 %–51 %) is observed. Note that weakly nonlinear theory (blue dots) captures the interface shape and the maximum height quite well for all the cases seen here. For parameters see: (*a*) case 3, (*b*) case 4, (*c*) case 5, (*d*) case 6 and (*e*) case 7 in table 3, grid (a) for all cases here. The percentage values for overshoot reported in each panel is calculated from data obtained from numerical simulations.

defined as

$$\frac{\hat{E}_{tot}}{g\left(\dfrac{\hat{R}_0}{l_q}\right)^2} \equiv E_{tot}(r, t) = E_{kin} + E_{pot}$$

$$= \int_{-\infty}^{\eta} \tfrac{1}{2}|\nabla\phi|^2 \,\mathrm{d}z + \tfrac{1}{2}\eta^2 + \sigma\left(\sqrt{1 + |\nabla_H \eta|^2} - 1\right). \tag{5.1}$$

Here $E_{tot}(r, t)$ satisfies the conservation equation $\partial E_{tot}/\partial t + \nabla_H \cdot \boldsymbol{F} = 0$ with the energy flux defined as $\boldsymbol{F}(r, t) \equiv -\int_{-\infty}^{\eta} (\nabla_H \phi)(\partial\phi/\partial t)\,\mathrm{d}z - \sigma[\partial\eta/\partial t(\nabla_H \eta)/\sqrt{1 + |\nabla_H \eta|^2}]$.

With $\nabla_H \equiv \boldsymbol{e}_r \partial/\partial r$ and $\nabla \equiv (\nabla_H, \partial/\partial z)$ and integrating the energy per unit area in (5.1) over the entire horizontal surface area, with the two-dimensional divergence theorem,

https://doi.org/10.1017/jfm.2020.851 Published online by Cambridge University Press

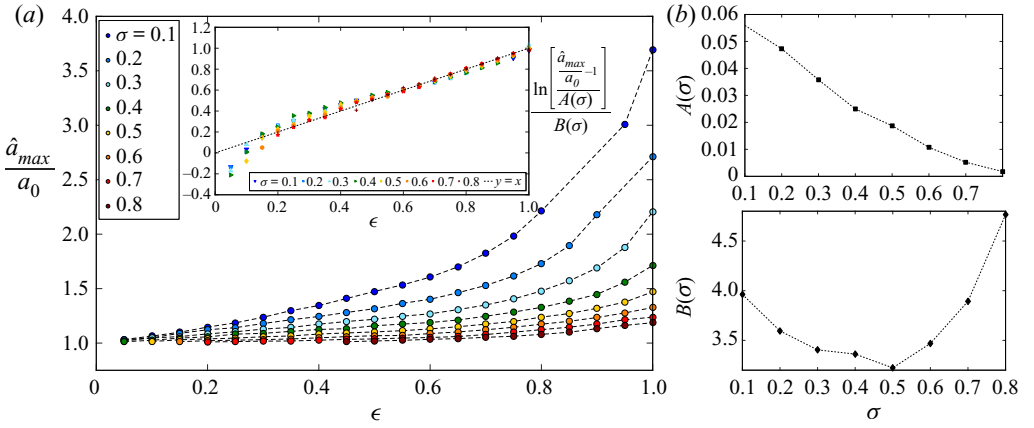

FIGURE 12. We define $\hat{a}_{max} \equiv \hat{\eta}(0, t_{max})$ where t_{max} is the instant when the jet reaches it maximum height. (*a*) Variation of $\hat{a}_{max}/a_0$ with ϵ for various values of σ (see legend), from numerical simulations. For moderate to large values of ϵ, the inset shows an approximate data collapse using the empirical relation $\hat{a}_{max}/a_0 = 1 + A(\sigma)\exp[B(\sigma)\epsilon]$. Note that $A(\sigma) \ll 1$ which ensures that $\hat{a}_{max}/a_0 \approx 1$ as $\epsilon \to 0$.

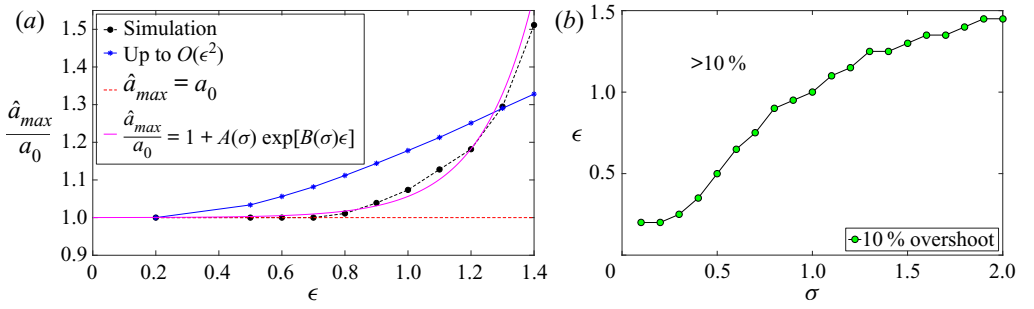

FIGURE 13. (*a*) Comparison of the variation of overshoot given by $(\hat{a}_{max}/a_0)$ with ϵ for $\sigma = 1.086$, $A(\sigma) = 1.562 \times 10^{-4}$ and $B(\sigma) = 5.8864$. It is seen that the weakly nonlinear theory (blue symbols) follows the qualitative trend seen in numerical simulations (black symbols). The solid (pink) line is $\hat{a}_{max}/a_0 = 1 + A(\sigma)\exp[B(\sigma)\epsilon]$ where the values of A and B are provided in the captions. (*b*) Simulation data. The curve is obtained from simulations and separates points where $>10\,\%$ overshoot is observed from those with $<10\,\%$ overshoot. It is clear from this curve that a higher value of ϵ is needed for jetting as surface tension is made stronger relative to gravity.

we see that $\boldsymbol{F}(l_q, t) = 0$ due to boundary conditions at the radial wall. We thus obtain the energy conservation condition $\mathrm{d}\mathcal{E}/\mathrm{d}t \equiv \mathrm{d}/\mathrm{d}t(\int_0^{l_q} E(r,t) r\,\mathrm{d}r) = 0$. At the linearised approximation, $E(r, t)$ has quadratic terms in ϵ whence it may be checked that $\mathcal{E}$ is a constant. In figure 14(*a*), we show comparisons of the potential energy (gravitational potential energy plus the surface energy) of the system as a function of time ($\mathcal{E}_0$ is the initial value of potential or total energy under each approximation) and a good agreement is seen, including that at the instant when the dimple becomes pronounced. In figure 14(*b*), we see the variation of total energy. Due to the truncation of $O(\epsilon^3)$ terms, the weakly nonlinear model does not conserve energy exactly and the oscillatory nature of these fluctuations is because we solve simple harmonic oscillator equations at every order. Figures 14(*a*) and 14(*b*) together imply that the weakly nonlinear model estimates

https://doi.org/10.1017/jfm.2020.851 Published online by Cambridge University Press

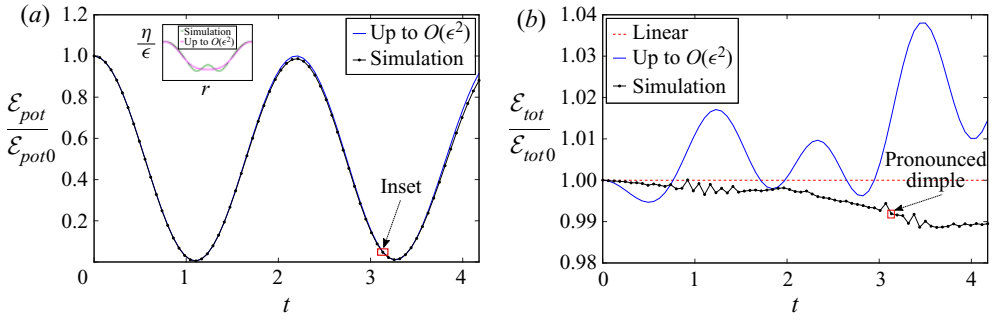

FIGURE 14. (*a*) Temporal variation of the ratio of instantaneous potential energy (surface energy + gravitational energy) $\mathcal{E}_{pot}$ to the initial potential energy $\mathcal{E}_{pot0}$ (see text below for definition of $\mathcal{E}$) with time t. The potential energy of the weakly nonlinear model (panel *a*) shows very good agreement with numerical simulations (inset shows when pronounced dimple forms). (*b*) Variation of total energy ($\mathcal{E}_{tot}/\mathcal{E}_{tot0}$) with time. The linearised approximation (dashed red line) is constant. The total energy of the weakly nonlinear solution (solid blue line) fluctuates in time (up to a maximum of $<4\,\%$) due to truncation of $O(\epsilon^3)$ terms. The increase in total energy at $t > 3.133$ is mainly due to overestimation of the velocity near the interface which causes an overestimation of the total kinetic energy (see figure 9).

the surface energy relatively more accurately than the kinetic energy, the latter being over-estimated by a maximum of around 4 %. This conclusion is also verified from the velocity profiles in figure 9, where close to the interface it is seen that the weakly nonlinear model overestimates the kinetic energy of the surface layer.

5.1. *Nonlinear redistribution of potential energy*

We have seen that while the weakly nonlinear prediction is able to describe dimple inception and jet overshoot, it does not resolve the formation of the pronounced dimple during the second half of the oscillation or the thinning of the neck of the jet which causes droplet pinchoff. Here, we use modal analysis to understand the reasons why this is so. The interface $\hat{\eta}$ may be expressed at any time $\hat{t}_0$ using the Dini series in (5.2) with coefficients $\hat{H}(l_j;\hat{t}_0)$ (related to the Hankel transform). Here $\hat{H}(l_j;\hat{t}_0)$ may be evaluated from (5.3) (Bagrov *et al.* 2012) using $\hat{\eta}(\hat{r},\hat{t}_0)$ obtained either from theory or simulations,

$$\hat{\eta}(\hat{r},\hat{t}_0) = \sum_{j=1}^{\infty} \hat{H}(l_j;\hat{t}_0)\mathrm{J}_0\left(l_j\frac{\hat{r}}{\hat{R}_0}\right), \tag{5.2}$$

$$\hat{H}(l_j;\hat{t}_0) \equiv \frac{1}{\frac{1}{2}\hat{R}_0^2\mathrm{J}_0^2(l_j)}\int_0^{\hat{R}_0}\hat{r}\hat{\eta}(\hat{r},\hat{t}_0)\mathrm{J}_0\left(l_j\frac{\hat{r}}{\hat{R}_0}\right)\mathrm{d}\hat{r}, \quad j = 1,2,3\ldots. \tag{5.3}$$

In (5.2) and (5.3), $|\hat{H}(l_j;\hat{t}_0)|$ may be thought of as a measure of the potential energy in mode j at time $\hat{t}_0$. In this study, we inject the entire initial energy as potential energy into the primary mode ($q = 5$). Nonlinearity subsequently causes a part of this energy to be redistributed to modes which did not have any energy to start with. It will be seen here that this redistribution plays a crucial role in dimple formation events. The integral in (5.3) is evaluated numerically for each j. Figures 15(*a*) and 15(*b*) show $|\hat{H}(l_j;\hat{t}_0)|$ at the inception of dimple formation and later when a pronounced dimple forms, respectively.

https://doi.org/10.1017/jfm.2020.851 Published online by Cambridge University Press

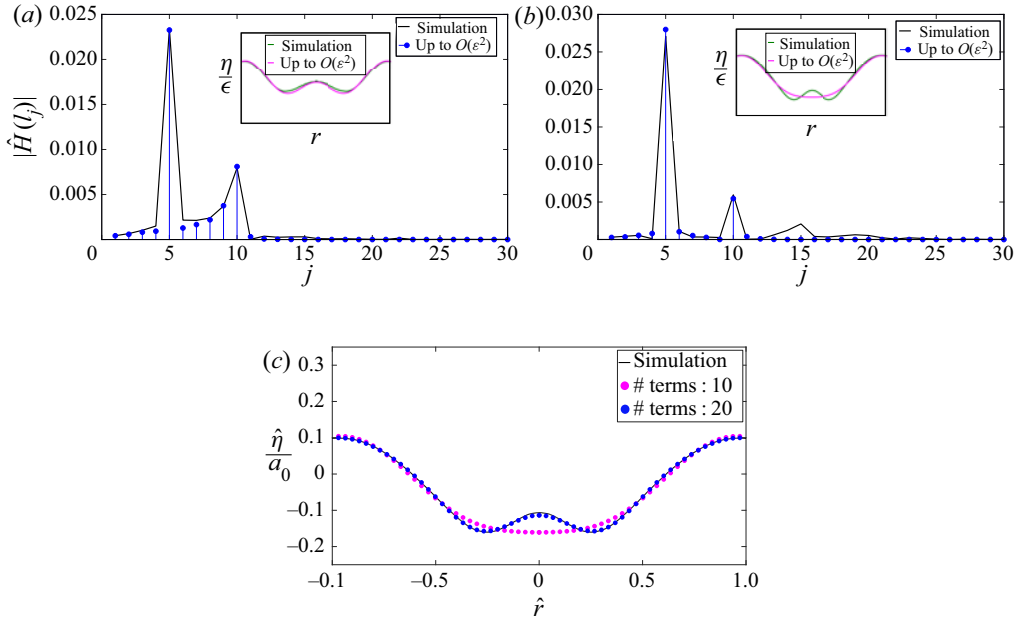

FIGURE 15. (*a*) Here $\hat{H}(l_j;\hat{t}_0)$ versus j ($\epsilon = 0.5$) at dimple inception, $\hat{t}_0 = 0.02$ s, see inset for interface. At this instant, the dimple is captured by theory as significant energy transfer has occurred up to $j = 10$ only. (*b*) Time $\hat{t}_0 = 0.051$ s. Dimple is sharper and narrower with significant surface energy in modes $> j = 10$ also, which is not captured by the $O(\epsilon^2)$ theory (*c*) Time $\hat{t}_0 = 0.051$ s. Interface shape obtained from (5.2) with $\hat{H}(l_j; 0.051)$ obtained from simulations up to $j = 10$ (pink symbols) and $j = 20$ (blue symbols) while the remaining are from theory (2.36).

It is seen that at dimple inception, a large number of modes up to $j = 10$ (second harmonic) share a sizeable fraction of the initial energy. At this time instant, the weakly nonlinear theory estimates the energy contained in the higher modes accurately leading to the good agreement for the dimple shape seen in the inset. At later time $\hat{t}_0 = 0.051$ s (figure 15*b*), when the dimple becomes more pronounced (narrower and sharper), many higher modes including noticeable peaks at $j = 15$ and 20 are seen. The potential energy for modes up to $j = 10$ is well predicted by the theory, but for larger j the theory suffers a significant error; this in turn leads to an unresolved dimple as seen in the inset of figure 15(*b*).

In order to analyse the unresolved dimple in figure 15(*b*) further, we perform a simple numerical test. In figure 15(*c*), we compare predictions from (5.2) where the first N values of $\hat{H}(l_j;\hat{t}_0)$ (i.e. $j = 1$ to N) have been obtained from simulations while the remainder ($j > N$) are from theory (2.36). It is seen clearly that in order to obtain the pronounced dimple seen in the inset of figure 15(*b*), one has to estimate $\hat{H}(l_j;\hat{t}_0)$ accurately up to $j = 20$. Correcting $\hat{H}(l_j;\hat{t}_0)$ up to $j = 10$ only in figure 15(*c*) is seen not to capture the shape of the dimple. This is consistent with the figure 15(*b*) where noticeable peaks are observed up to $j = 20$.

Similar conclusions may be drawn from figure 16 where $\epsilon = 1.2$. It is seen in figure 16(*a*) that at $\hat{t}_0 = 0.02$ s, dimple initiation is well described by the weakly nonlinear model as significant energy transfer has occurred up to $j = 10$ only. However, pronounced dimple formation is not well resolved later at $\hat{t}_0 = 0.05$ s in figure 16(*b*). The spread of

https://doi.org/10.1017/jfm.2020.851 Published online by Cambridge University Press

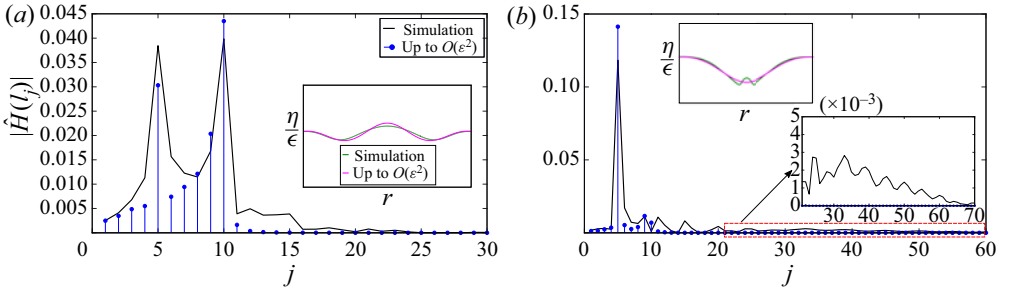

FIGURE 16. (*a*) Here $\hat{H}(l_j; \hat{t}_0)$ versus j at first dimple formation ($\epsilon = 1.2$), $\hat{t}_0 = 0.02$ s. (*a*) Significant energy transfer has occurred only up to modes $\leq j = 10$. (*b*) A pronounced dimple with significant potential energy in modes $> j = 10$, $\hat{t}_0 = 0.05$ s.

the energy becomes more delocalised now with small but noticeable potential energy in modes up to $j = 50$ in figure 16(*b*), see lower inset.

We have seen that the dimple becomes narrower with energy transfer to an increasingly broader set of modes, as ϵ is increased. The widest pronounced dimple seen in the present analysis is $\approx$4.2 mm wide (for $\epsilon = 0.5$) and thus well below the air–water capillary-gravity wavelength of $\approx$17 mm. Consequently, these dimples can be treated as pure capillary waves, despite the primary perturbation being a much longer capillary-gravity wave. Our weakly nonlinear model is unable to capture the time evolution of the dimple due to its inability to resolve energy transfer beyond $j = 10$. Despite this limitation, at the end of one oscillation when the jet is close to its maximum height, the local shape of the jet around $\hat{r} = 0$ is well approximated by the nonlinear theory (see figure 11*a–e*). In order to understand this apparent paradoxical behaviour, $\hat{H}(l_j; \hat{t}_0)$ versus j is plotted close to the instant of maximum jet height, in figures 17(*a*) and 17(*b*). It is seen that the maximum height of the jet is well described by the theory but the 'shoulders' of the jet are not. It may thus be inferred that in order to obtain the maximum height of the jet accurately, lower mode contributions ($j = 1$–10) are important which our $O(\epsilon^2)$ analysis achieves quite accurately. In contrast, in order to get the entire jet shape accurately, the 'shoulder' also needs to be resolved. This requires accurate estimation of higher-mode coefficients which require corrections presumably at $O(\epsilon^3)$ and $O(\epsilon^4)$. To sum up what we learn from this analysis so far, a short tabular summary of the relative strengths and weaknesses of the nonlinear model is provided in table 4.

6. Critical values of σ: a special case of triadic resonance

The expressions for η, ϕ and Ω_2 in (2.33), (2.36) and (2.37) are singular at certain critical values of σ. This is easily seen from the denominators of the expressions in appendix B, where singularities occur when $\omega_k = 2\omega_q$. With the definition $\omega_k^2 = \alpha_k(1 + \sigma\alpha_k^2)$, this leads to the set of critical values of σ *viz.*

$$\sigma_c^{(k)} = \frac{4 - \alpha_k}{\alpha_k^3 - 4}, \quad k = 1, 2, 3 \ldots . \tag{6.1a,b}$$

This is the cylindrical analogue of the well-known second harmonic resonance condition known in the case of Wilton ripples (Wilton 1915). In two-dimensional Cartesian geometry, second harmonic resonance for capillary-gravity waves was analysed first by

https://doi.org/10.1017/jfm.2020.851 Published online by Cambridge University Press

Strengths	Weaknesses
(i) Captures energy transfer from the primary capillary-gravity mode to small-scale pure capillary modes in the spectrum, in agreement with numerical simulations. Reasonably accurate estimate of energy transfer to modes up to the second harmonic (see figures 15*a* and 16*a*).	(i) The $O(\epsilon^2)$ theory does not capture energy transfer to modes beyond the second (spatial) harmonic (i.e. $j > 10$ in this study) (see figures 15*b* and 16*b*). Energy transfer to higher modes ($j \geq 10$) (figures 15*b* and 16*b*) requires $O(\epsilon^3)$ and higher-order corrections.
(ii) Captures initiation of dimple formation (figures 7*b* and 8*c*), qualitative aspects of velocity (figures 9*a* and 9*b*) and pressure profiles (figures 10*a* and 10*c*) at dimple inception and at maximum jet height. Predicts the overshoot of the jet to within 10 % accuracy (figure 13*a*) and the jet shape at its tip at maximum overshoot (figure 11)	(ii) Time evolution of pronounced dimple including its narrowing, thinning of the neck and developing into a slender jet and pressure profile at pronounced dimple is not captured (figures 8*f*, 8*g* and 10*b*, respectively).
(iii) Captures aforementioned qualitative features even beyond $\epsilon > 1$. Total surface energy quite accurate for moderate ϵ (figure 14*a*). Assigns the contribution of higher-order modes to various jet attributes, e.g. maximum height ($j \leq 10$), shoulder ($j \geq 10$), etc.	(iii) The $O(\epsilon^2)$ theory loses accuracy at large ϵ, necessitating higher-order corrections. Energy is not conserved exactly (due to truncation) and due to this, the nonlinear model overestimates the liquid layer velocities near the surface (at moderate ϵ) with fluctuations in total energy up to 4 % (figure 14*b*).
(iv) Singularities in σ points to possibility of bifurcations and instabilities at critical values of σ due to triadic resonant interactions in a cylindrical confined geometry (see § 6)	(iv) Theory diverges at the critical σ making a series of σ values inaccessible. Near these σ, the theory needs reformulation (see § 6).
(v) A systematic method for higher-order approximations. Leads to analytical expressions which can be efficiently evaluated, e.g. $\eta(r, t)$ in (2.36) evaluates within a few minutes on a desktop computer, for one oscillation.	(v) Nonlinear derivation is mathematically laborious, and obtaining $O(\epsilon^3)$ and higher-order corrections, although conceptually not significantly more difficult, requires lengthy algebra.
(vi) Offers an alternative approach to understanding jetting and dimple formation complementing earlier insights based on wave-focussing, singularity, self-similar solutions and scaling analysis. An analogy of our approach may be drawn with studies investigating the steepest standing wave (in Cartesian geometry) which can develop a cusp (singularity) at its peak (cf. classical studies by Lord Rayleigh (Strutt 1915) and G. I. Taylor (1953) and the perturbative expansions by Price & Penneyand (1952) and Schwartz & Whitney (1981))	(vi) The curvature is not singular at dimple inception in the model. Accessing this singularity presumably requires higher-order corrections.

TABLE 4. Strengths and weaknesses of the $O(\epsilon^2)$ solution to the IVP.

https://doi.org/10.1017/jfm.2020.851 Published online by Cambridge University Press

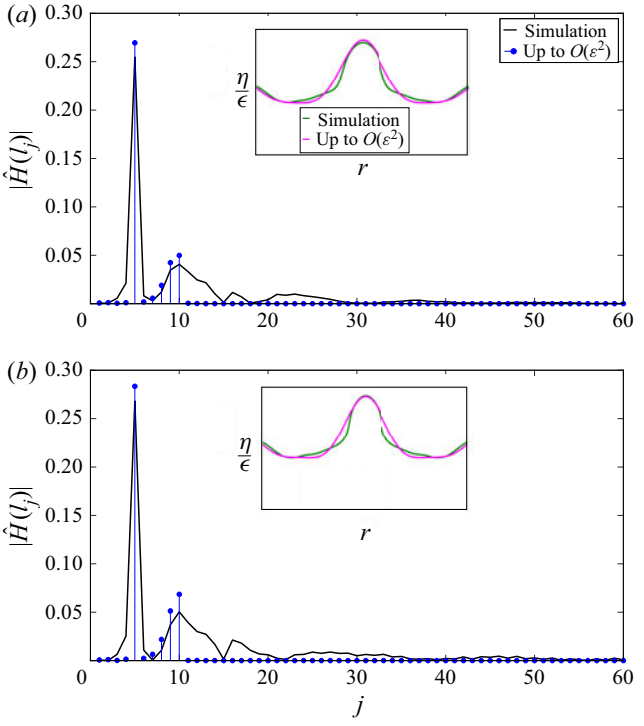

FIGURE 17. Here $\hat{H}(l_j; \hat{t}_0)$ versus j when the jet is at its maximum height: (*a*) $\epsilon = 1.2$; (*b*) $\epsilon = 1.3$. As seen from the jet shape in the insets, the nonlinear model estimates the maximum height of the jet well but not the 'shoulder' of the jet, instead developing a broader base. It is concluded that in order to predict maximum height, one needs to estimate potential energy in modes up to $j = 10$ only which the theory does well. However, for resolving the jet 'shoulder', one has to estimate the potential energy in modes $> j = 10$ accurately which the $O(\epsilon^2)$ theory cannot capture. Here $\hat{t}_0 = 0.067$ s.

Wilton (1915) and since then has been studied extensively in Cartesian geometry (see Christodoulides & Dias (1994) for a compilation of the literature). In the same notation as used here with $j \in \mathbb{Z}^+$ as index for the Fourier modes $\cos(jx)$ and $j = 1$ being the primary mode, the Cartesian dispersion relation for capillary-gravity waves is $\omega(j) = \sqrt{j(1 + j^2\sigma)}$. The second harmonic resonance condition $\omega(2) = 2\omega(1)$ leads to a single critical value of σ, *viz.* $\sigma = \frac{1}{2}$. This is due to the fact that at $O(\epsilon^2)$, the product of the primary mode, *viz.* $\cos^2(x)$, has projections on only the zeroth and the second Fourier modes, i.e. $\cos^2(x) = \frac{1}{2}[\cos(0x) + \cos(2x)]$. This leads to a single critical value $\sigma_c = \frac{1}{2}$ at this order. In contrast, in the cylindrical axisymmetric geometry studied here, the product of the primary mode, *viz.* $\mathrm{J}_0^2(r)$, has projections on every mode in the spectrum, *viz.* $\mathrm{J}_0^2(r) = \sum_{k=0}^{\infty} c_k \mathrm{J}_0(\alpha_k r)$ $(k = 1, 2, 3 \ldots)$. This leads to a countably infinite sequence of critical values for $\sigma_c^{(k)}$ out of which, we are interested in positive values only. These critical values of σ are plotted in figure 18 for three different choices of the primary mode $q = 2, 5$ and 7. It is seen that for every q, there is an upper limit on $\sigma_c^{(k)}$. In this study for comparisons with weakly nonlinear predictions, we have chosen σ to be far from these singular values. For the case $q = 5$ studied here, $\sigma = 1.086$ (indicated with a dotted line in figure 18) is chosen to be far from the two neighbouring critical values of σ. This order of

https://doi.org/10.1017/jfm.2020.851 Published online by Cambridge University Press

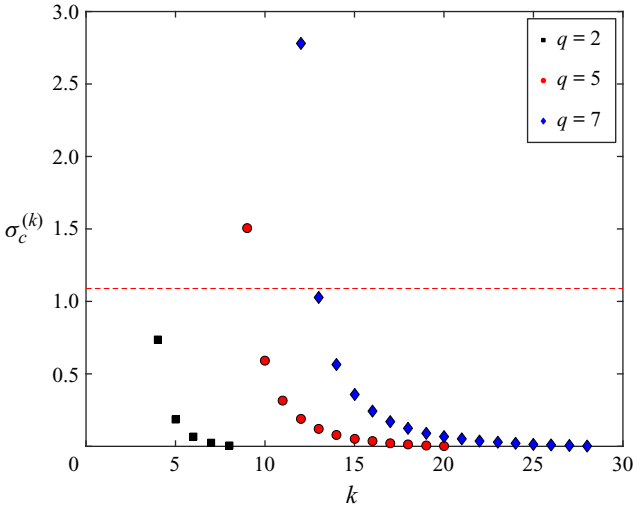

FIGURE 18. Critical values $\sigma_c^{(k)}$ for various choices of the primary mode q. In this study we have chosen $\sigma = 1.086$ (dotted red line) which is far from the two neighbouring critical values of sigma, indicated by red dots for $q = 5$.

magnitude is consistent with our necessity of $\sigma = O(1)$ for $\epsilon \to 0$, see discussion above (2.14).

It is known that the second harmonic resonance condition arises only when capillarity as well as gravity are accounted for in the nonlinear calculation. This is due to the existence of a minimum in the linearised phase speed for capillary-gravity waves (McGoldrick 1970). At any speed above this minimum, there is a certain wavenumber at which the primary mode and its second harmonic travel at the same speed leading to resonance. For air–water parameters, the critical wavenumber corresponding to this occurs at a wavelength of approximately 2.44 cm, in two-dimensional Cartesian geometry. Since two-dimensional Cartesian, $(\eta(x, \tau) \propto \cos(kx))$, and cylindrical axisymmetric surface waves, $(\eta(r, \tau) \propto \mathrm{J}_0(kr))$, share the same dispersion relation at linear order, it is natural to expect this resonance to also occur in cylindrical geometry. As a consistency check, when we consider pure gravity axisymmetric waves, the condition $\omega_k = 2\omega_q$ leads to $\alpha_k = 4$, while for pure capillary axisymmetric waves, the same condition leads to $\alpha_k = 4^{1/3} \approx 1.5874$. It may be checked numerically that these relations cannot be exactly satisfied by the ratio of any two non-trivial roots of $\mathrm{J}_1(\alpha_j) = 0$, demonstrating that second harmonic resonance is not possible for pure capillary or pure gravity waves in cylindrical, axisymmetric geometry.

Finally, we note that in Cartesian geometry, the second harmonic resonance condition is easily seen to be a special case of the triadic resonance condition $\omega(1) + \omega(1) - \omega(2) = 0$ and $1 + 1 - 2 = 0$, where two of the members in the triad are the primary modes (repeated) and the third member is the second harmonic of the primary mode (McGoldrick 1970). Interestingly in cylindrical confined geometry, this resonance condition depends not only on the fluid properties and the primary mode chosen, but also on the size of the container $\hat{R}_0$, e.g. for each the symbols in red corresponding to $q = 5$ in figure 18, a condition of the form $2\omega_5 = \pm\omega_9$, $2\omega_5 = \pm\omega_{10}, \ldots, 2\omega_5 = \pm\omega_{21}$ is satisfied (see Natarajan & Brown (1986) for similar conditions for second harmonic resonance for capillary oscillations of a liquid spherical droplet). Each of these relations leads to a critical value of $\hat{R}_0$ for air–water parameters. As there are finite number of critical points

https://doi.org/10.1017/jfm.2020.851 Published online by Cambridge University Press

for any q (see figure 18), there is consequently an upper and lower limit on $\hat{R}_0$. For air–water parameters and $q = 5$ we obtain $\hat{R}_0^{min} = 3.64$ cm and $\hat{R}_0^{max} = 87.98$ cm. Radii larger or smaller than these upper and lower values are free from singularities at this order. In the vicinity of the critical points, our weakly nonlinear solution ceases to be uniformly valid and needs to be reformulated, and this is proposed as future work.

7. Conclusions

In this study, we have investigated jetting from finite amplitude, axisymmetric capillary-gravity waves on a deep cylindrical pool, using a first principles weakly nonlinear analysis. The primary conclusions are as follows.

(i) Jets may be obtained from smooth initial perturbations. These are large amplitude, surface perturbations on a deep liquid pool which produce nonlinear axisymmetric, capillary-gravity waves and a subsequent jet. The jet shares some of its attributes to those seen in bubble bursting and other similar cavity collapse phenomena. Analogous to the latter, the birth of the jet commences as a dimple (with associated curvature reversal) at the wave trough. The dimple width (at inception) varies inversely while the velocity at its tip varies directly with ϵ.

(ii) At large ϵ when well formed, slender jets are obtained, the acceleration at the base of the dimple can exceed gravity by nearly an order of magnitude (see accompanying supplementary material for acceleration plots). The birth of the jet is thus predominantly a capillary event, despite the parent perturbation being a capillary-gravity wave.

(iii) The formation of this jet, right from its inception as a dimple to becoming a well-formed jet, is a nonlinear process. Its inception and subsequent evolution involve energy transfer to a large number of harmonics of the primary mode along with many intermediate modes. Some of the jet features, e.g. dimple inception, the maximum height reached and its shape around $\hat{r} = 0$, require an accurate description of energy transfer only up to the second harmonic, and are well described by the $O(\epsilon^2)$ calculation. Other features such as dimple evolution, thinning of the neck leading to a slender jet with droplet pinchoff, involve energy transfer to an increasingly broader band of modes, as ϵ is increased. Describing the energy in these high modes accurately requires higher-order corrections and cannot be captured by the theory presented here.

(iv) The weakly nonlinear theory is able to capture the qualitative dependence of the jet overshoot on ϵ. Quantitative differences between theory and simulations up to a maximum of $\approx 10\,\%$ exist. The maximum height of the jet and its local shape around $\hat{r} = 0$ are captured with reasonable accuracy in the range $\epsilon \in [0.2\text{–}1.2]$ with $\sigma = O(1)$.

(v) There exists a finite number of critical values of σ where the weakly nonlinear theory is singular. These critical points are the cylindrical analogues of the corresponding singularities known in the case of Wilton ripples (Wilton 1915) and are a special case of triadic resonance (McGoldrick 1970; Hammack & Henderson 1993). The possibility of instabilities at these critical values of σ requires a detailed investigation planned in the near future.

Certain attributes have been neglected in our analysis but will nevertheless retain an important role in the physics of jetting. Firstly, we have not taken into account the role of viscosity (μ). Figures 12 and 13(b) maybe visualised as a slice obtained for zero Ohnesorge

https://doi.org/10.1017/jfm.2020.851 Published online by Cambridge University Press

number (Oh) which in this case can be defined as $Oh \equiv \mu/\sqrt{\rho T a_0}$ (square of an inverse Laplace number (Deike *et al.* 2018)). It was first shown by Duchemin *et al.* (2002) that the jet velocity has a non-monotonic dependence on viscosity, increasing initially with increasing viscosity but showing a peak at a critical value of viscosity (see figure 12 in Duchemin *et al.* (2002)). A predictive model of jetting recently proposed in Gordillo & Rodríguez-Rodríguez (2019) and validated through direct numerical simulations in Blanco-Rodríguez & Gordillo (2020) supports this conclusion, where the jet velocity increases as $Oh^{1/2}$ before reaching a peak at a critical Oh_c and subsequently decreasing as Oh^{-1}. These interesting predictions need to be tested on the jets reported here using a nonlinear viscous IVP solution. A viscous analysis is also expected to be free from the singularities in σ that are obtained here. A related physics not taken into account is the dissipation at the three-phase contact line which will be encountered in the confined cylindrical geometry studied here. As has been shown recently in Viola, Brun & Gallaire (2018), capillary effects are particularly important in the limit of small amplitude waves. We conclude with the observation that the present study is a first step towards solving the IVP for jetting from a collapsing cavity. While we have investigated the physics of jetting formed from a single Fourier–Bessel mode, tools, results and insights presented here are of utility in investigating the nonlinear IVP, when a spectrum of modes are present in the initial perturbation. These studies are underway and will be reported subsequently.

Acknowledgements

We thank R. Govindarajan for helpful comments. Financial support from Science and Engineering Research Board (Department Science and Technology (DST)), Government of India (# EMR/2016/000830) and Industrial Research and Consultancy Centre, IIT Bombay is acknowledged. P.K.F.'s doctoral fellowship and Research Assistantship (2014–2020) was supported by a seed grant from IRCC, IIT Bombay. S.B. acknowledges the Prime Minister's Research Fellowship (PMRF, Government of India) for funding. We thank Dr S. Popinet for permission to set up a test case on the Basilisk server.

Declaration of interests

The authors report no conflict of interest.

Supplementary material and movies

Supplementary material and movies are available at https://doi.org/10.1017/jfm.2020.851.

Appendix A

The expressions for inhomogenous terms $F_i(r,\tau)$ and $G_i(r,\tau)$ in (2.25) and (2.26) are

$$F_1(r,\tau)=0, \quad F_2(r,\tau)=-\left[\eta_1\left(\frac{\partial^2\phi_1}{\partial z\partial\tau}\right)+\frac{1}{2}\left\{\left(\frac{\partial\phi_1}{\partial r}\right)^2+\left(\frac{\partial\phi_1}{\partial z}\right)^2\right\}\right]_{z=0}, \quad \text{(A 1}a,b\text{)}$$

https://doi.org/10.1017/jfm.2020.851 Published online by Cambridge University Press

$$F_3(r,\tau) = -\left[\eta_2\left(\frac{\partial^2\phi_1}{\partial z\partial\tau}\right) + \frac{\eta_1^2}{2}\left(\frac{\partial^3\phi_1}{\partial z^2\partial\tau}\right) + \eta_1\left(\frac{\partial^2\phi_2}{\partial z\partial\tau}\right) + \eta_1\left(\frac{\partial\phi_1}{\partial r}\right)\left(\frac{\partial^2\phi_1}{\partial r\partial z}\right)\right.$$
$$+\eta_1\left(\frac{\partial\phi_1}{\partial z}\right)\left(\frac{\partial^2\phi_1}{\partial z^2}\right) + \left(\frac{\partial\phi_1}{\partial r}\right)\left(\frac{\partial\phi_2}{\partial r}\right) + \left(\frac{\partial\phi_1}{\partial z}\right)\left(\frac{\partial\phi_2}{\partial z}\right)$$
$$\left. + \Omega_2\left(\frac{\partial\phi_1}{\partial\tau}\right)\right]_{z=0} - \frac{\sigma}{2}\left[3\left(\frac{\partial^2\eta_1}{\partial r^2}\right)\left(\frac{\partial\eta_1}{\partial r}\right)^2 + \frac{1}{r}\left(\frac{\partial\eta_1}{\partial r}\right)^3\right], \tag{A 2}$$

$$G_1(r,\tau) = 0, \tag{A 3}$$

$$G_2(r,\tau) = -\left[\eta_1\left(\frac{\partial^3\phi_1}{\partial z\partial\tau^2}\right) + \eta_1\left(\frac{\partial^2\phi_1}{\partial z^2}\right) + \frac{\partial}{\partial\tau}\left\{\left(\frac{\partial\phi_1}{\partial r}\right)^2 + \left(\frac{\partial\phi_1}{\partial z}\right)^2\right\}\right]_{z=0}$$
$$+\sigma\left[\left(\frac{\partial\phi_1}{\partial r}\right)\left\{\left(\frac{\partial^3\eta_1}{\partial r^3}\right) + \frac{1}{r}\left(\frac{\partial^2\eta_1}{\partial r^2}\right) - \frac{1}{r^2}\left(\frac{\partial\eta_1}{\partial r}\right)\right\}\right]_{z=0}, \tag{A 4}$$

$$G_3(r,\tau) = -\left[\eta_2\left(\frac{\partial^3\phi_1}{\partial z\partial\tau^2}\right) + \frac{\eta_1^2}{2}\left(\frac{\partial^4\phi_1}{\partial z^2\partial\tau^2}\right) + \eta_1\left(\frac{\partial^3\phi_2}{\partial z\partial\tau^2}\right) + \eta_2\left(\frac{\partial^2\phi_1}{\partial z^2}\right)\right.$$
$$+\frac{\eta_1^2}{2}\left(\frac{\partial^3\phi_1}{\partial z^3}\right) + \eta_1\left(\frac{\partial^2\phi_2}{\partial z^2}\right) + 2\eta_1\left(\frac{\partial\phi_1}{\partial r}\right)\left(\frac{\partial^3\phi_1}{\partial\tau\partial r\partial z}\right)$$
$$+2\eta_1\left(\frac{\partial^2\phi_1}{\partial r\partial z}\right)\left(\frac{\partial^2\phi_1}{\partial\tau\partial r}\right) + 2\eta_1\left(\frac{\partial\phi_1}{\partial z}\right)\left(\frac{\partial^3\phi_1}{\partial\tau\partial z^2}\right) + 2\eta_1\left(\frac{\partial^2\phi_1}{\partial z^2}\right)\left(\frac{\partial^2\phi_1}{\partial\tau\partial z}\right)$$
$$+2\left(\frac{\partial\phi_2}{\partial r}\right)\left(\frac{\partial^2\phi_1}{\partial\tau\partial r}\right) + 2\left(\frac{\partial\phi_1}{\partial r}\right)\left(\frac{\partial^2\phi_2}{\partial\tau\partial r}\right) + 2\left(\frac{\partial\phi_2}{\partial z}\right)\left(\frac{\partial^2\phi_1}{\partial\tau\partial z}\right)$$
$$+2\left(\frac{\partial\phi_1}{\partial z}\right)\left(\frac{\partial^2\phi_2}{\partial\tau\partial z}\right) + \frac{1}{2}\left(\frac{\partial\phi_1}{\partial r}\right)\frac{\partial}{\partial r}\left\{\left(\frac{\partial\phi_1}{\partial r}\right)^2 + \left(\frac{\partial\phi_1}{\partial z}\right)^2\right\}$$
$$\left.+\frac{1}{2}\left(\frac{\partial\phi_1}{\partial z}\right)\frac{\partial}{\partial z}\left\{\left(\frac{\partial\phi_1}{\partial r}\right)^2 + \left(\frac{\partial\phi_1}{\partial z}\right)^2\right\} + 2\Omega_2\left(\frac{\partial^2\phi_1}{\partial\tau^2}\right)\right]_{z=0}$$
$$+\sigma\left[-\frac{3}{2}\left(\frac{\partial\eta_1}{\partial r}\right)^2\left\{\left(\frac{\partial^3\eta_1}{\partial\tau\partial r^2}\right) + \frac{1}{r}\left(\frac{\partial^2\eta_1}{\partial\tau\partial r}\right)\right\} - 3\left(\frac{\partial^2\eta_1}{\partial\tau\partial r}\right)\left(\frac{\partial^2\eta_1}{\partial r^2}\right)\left(\frac{\partial\eta_1}{\partial r}\right)\right.$$
$$+\left(\frac{\partial\phi_1}{\partial r}\right)_{z=0}\left\{\left(\frac{\partial^3\eta_2}{\partial r^3}\right) + \frac{1}{r}\left(\frac{\partial^2\eta_2}{\partial r^2}\right) - \frac{1}{r^2}\left(\frac{\partial\eta_2}{\partial r}\right)\right\}$$
$$+\eta_1\left(\frac{\partial^2\phi_1}{\partial z\partial r}\right)_{z=0}\left\{\left(\frac{\partial^3\eta_1}{\partial r^3}\right) + \frac{1}{r}\left(\frac{\partial^2\eta_1}{\partial r^2}\right) - \frac{1}{r^2}\left(\frac{\partial\eta_1}{\partial r}\right)\right\}$$
$$+\left(\frac{\partial\phi_2}{\partial r}\right)_{z=0}\left\{\left(\frac{\partial^3\eta_1}{\partial r^3}\right) + \frac{1}{r}\left(\frac{\partial^2\eta_1}{\partial r^2}\right) - \frac{1}{r^2}\left(\frac{\partial\eta_1}{\partial r}\right)\right\}$$
$$\left.+\Omega_2\left\{\left(\frac{\partial^3\eta_1}{\partial\tau\partial r^2}\right) + \frac{1}{r}\left(\frac{\partial^2\eta_1}{\partial\tau\partial r}\right)\right\}\right]. \tag{A 5}$$

https://doi.org/10.1017/jfm.2020.851 Published online by Cambridge University Press

Appendix B

At $O(\epsilon^2)$ the solution is given by

$$\eta_2(r,\tau) = \sum_{k=1}^{\infty}\left[\zeta_1^{(k)}\cos(\omega_k\tau) + \zeta_2^{(k)}\cos(2\omega_q\tau) + \zeta_3^{(k)}\right]\mathrm{J}_0(\alpha_k r), \tag{B 1}$$

$$\phi_2(r,\tau) = \frac{\mathrm{J}_0^2(l_q)}{2}\sin\left(2\omega_q\tau\right) + \sqrt{1+\sigma}\sum_{k=1}^{\infty}\left[\xi_1^{(k)}\sin\left(\omega_k\tau\right) + \xi_2^{(k)}\sin\left(2\omega_q\tau\right)\right]\mathrm{J}_0\left(\alpha_k r\right)\exp\left(\alpha_k z\right), \tag{B 2}$$

where

$$\zeta_1^{(k)} = -\frac{2\left(1+\sigma\right)}{\mathrm{J}_0^2(l_k)\left(1+\alpha_k^2\sigma\right)\left(\omega_k^2-4\omega_q^2\right)}\left\{\left[\left(\alpha_k-2\right)+\left(\alpha_k^3-\alpha_k^2-1\right)\sigma\right]I_{0-k,0-q,0-q} + \left[2+\left(1+\alpha_k^2\right)\sigma\right]I_{0-k,1-q,1-q}\right\}, \tag{B 3}$$

$$\zeta_2^{(k)} = \frac{1+\sigma}{2\mathrm{J}_0^2(l_k)\left(1+\alpha_k^2\sigma\right)\left(\omega_k^2-4\omega_q^2\right)}\left\{\left[\left(3\alpha_k-4\right)+\left(3\alpha_k^3-4\alpha_k^2\right)\sigma\right]I_{0-k,0-q,0-q} + \left[\left(4+\alpha_k\right)+\left(\alpha_k^3+4\alpha_k^2\right)\sigma\right]I_{0-k,1-q,1-q}\right\}, \tag{B 4}$$

$$\zeta_3^{(k)} = \frac{1+\sigma}{2\mathrm{J}_0^2(l_k)\left(1+\alpha_k^2\sigma\right)}\left\{I_{0-k,0-q,0-q} - I_{0-k,1-q,1-q}\right\} \tag{B 5}$$

and

$$\xi_1^{(k)} = \frac{2\omega_q}{\mathrm{J}_0^2(l_k)\omega_k\left(\omega_k^2-4\omega_q^2\right)}\left\{\left[\left(\alpha_k-2\right)+\left(\alpha_k^3-\alpha_k^2-1\right)\sigma\right]I_{0-k,0-q,0-q} + \left[2+\left(1+\alpha_k^2\right)\sigma\right]I_{0-k,1-q,1-q}\right\}, \tag{B 6}$$

$$\xi_2^{(k)} = -\frac{\left\{\left[2+\left(3-\alpha_k^2\right)\sigma\right]I_{0-k,0-q,0-q} + \left[2+\left(1+\alpha_k^2\right)\sigma\right]I_{0-k,1-q,1-q}\right\}}{\mathrm{J}_0^2(l_k)\left(\omega_k^2-4\omega_q^2\right)}. \tag{B 7}$$

REFERENCES

AGBAGLAH, G., DELAUX, S., FUSTER, D., HOEPFFNER, J., JOSSERAND, C., POPINET, S., RAY, P., SCARDOVELLI, R. & ZALESKI, S. 2011 Parallel simulation of multiphase flows using octree adaptivity and the volume-of-fluid method. *CR Mecanique* **339** (2–3), 194–207.

ANTKOWIAK, A., BREMOND, N., LE DIZÈS, S. & VILLERMAUX, E. 2007 Short-term dynamics of a density interface following an impact. *J. Fluid. Mech.* **577**, 241–250.

BAGROV, V. G, BELOV, A. A., ZADOROZHYNI, V. N. & TRIFONOV, A. YU. 2012 Methods of mathematical physics-special functions. http://portal.tpu.ru:7777/SHARED/a/ATRIFONOV/eng/academics/Tab3/FTI_Bagrov_Belov_Zadorozhnyi_Trifonov_EMathPh-1e.pdf.

BARTOLO, D., JOSSERAND, C. & BONN, D. 2006 Singular jets and bubbles in drop impact. *Phys. Rev. Lett.* **96** (12), 124501.

BASAK, S., FARSOIYA, P. & DASGUPTA, R. 2020 Nonlinear capillary-gravity wave. http://basilisk.fr/sandbox/farsoiya/capillary_gravity_jetting.c, [Online; accessed 12-June-2020].

BELL, J. B, COLELLA, P. & GLAZ, H. M. 1989 A second-order projection method for the incompressible Navier–Stokes equations. *J. Comput. Phys.* **85** (2), 257–283.

https://doi.org/10.1017/jfm.2020.851 Published online by Cambridge University Press

BLAKE, J. R. & GIBSON, D. C. 1981 Growth and collapse of a vapour cavity near a free surface. *J. Fluid Mech.* **111**, 123–140.

BLANCHARD, D. C. 1963 The electrification of the atmosphere by particles from bubbles in the sea. *Prog. Oceanogr.* **1**, 73–202.

BLANCHARD, D. C. 1989 The size and height to which jet drops are ejected from bursting bubbles in seawater. *J. Geophys. Res.: Oceans* **94** (C8), 10999–11002.

BLANCHARD, D. C. 2004 *From Raindrops to Volcanoes: Adventures with Sea Surface Meteorology*. Courier Corporation.

BLANCHARD, D. C. & SYZDEK, L. D. 1972 Concentration of bacteria in jet drops from bursting bubbles. *J. Geophys. Res.* **77** (27), 5087–5099.

BLANCO-RODRÍGUEZ, F. J. & GORDILLO, J. M. 2020 On the sea spray aerosol originated from bubble bursting jets. *J. Fluid Mech.* **886**, R2.

BOULTON-STONE, J. M. & BLAKE, J. R. 1993 Gas bubbles bursting at a free surface. *J. Fluid Mech.* **254**, 437–466.

BRACKBILL, J. U., KOTHE, D. B. & ZEMACH, C. 1992 A continuum method for modeling surface tension. *J. Comput. Phys.* **100** (2), 335–354.

CASTILLO-OROZCO, E., DAVANLOU, A., CHOUDHURY, P. K. & KUMAR, R. 2015 Droplet impact on deep liquid pools: Rayleigh jet to formation of secondary droplets. *Phys. Rev.* E **92** (5), 053022.

CHENY, J. M. & WALTERS, K. 1996 Extravagant viscoelastic effects in the worthington jet experiment. *J. Non-Newtonian Fluid Mech.* **67**, 125–135.

CHRISTODOULIDES, P. & DIAS, F. 1994 Resonant capillary–gravity interfacial waves. *J. Fluid Mech.* **265**, 303–343.

DAS, S. P. & HOPFINGER, E. J. 2008 Parametrically forced gravity waves in a circular cylinder and finite-time singularity. *J. Fluid Mech.* **599**, 205–228.

DASGUPTA, R., TOMAR, G. & GOVINDARAJAN, R. 2015 Numerical study of laminar, standing hydraulic jumps in a planar geometry. *Eur. Phys. J.* E **38** (5), 45.

DEBNATH, L. 1994 *Nonlinear Water Waves*. Academic Press.

DEIKE, L., GHABACHE, E., LIGER-BELAIR, G., DAS, A. K, ZALESKI, S., POPINET, S. & SÉON, T. 2018 Dynamics of jets produced by bursting bubbles. *Phys. Rev. Fluids* **3** (1), 013603.

DHAR, M., DAS, G. & DAS, P. K. 2020 Planar hydraulic jumps in thin film flow. *J. Fluid Mech.* **884**, A11.

DUCHEMIN, L., POPINET, S., JOSSERAND, C. & ZALESKI, S. 2002 Jet formation in bubbles bursting at a free surface. *Phys. Fluids* **14** (9), 3000–3008.

FARSOIYA, P. K., MAYYA, Y. S. & DASGUPTA, R. 2017 Axisymmetric viscous interfacial oscillations–theory and simulations. *J. Fluid Mech.* **826**, 797–818.

FULTZ, D. & MURTY, T. S. 1963 Experiments on the frequency of finite-amplitude axisymmetric gravity waves in a circular cylinder. *J. Geophys. Res.* **68** (5), 1457–1462.

FUSTER, D. & POPINET, S. 2018 An all-mach method for the simulation of bubble dynamics problems in the presence of surface tension. *J. Comput. Phys.* **374**, 752–768.

GAÑÁN-CALVO, A. M. 2017 Revision of bubble bursting: universal scaling laws of top jet drop size and speed. *Phys. Rev. Lett.* **119** (20), 204502.

GAÑÁN-CALVO, A. M. 2018*a* Gañán-calvo replies. *Phys. Rev. Lett.* **121** (26), 269402.

GAÑÁN-CALVO, A. M. 2018*b* Scaling laws of top jet drop size and speed from bubble bursting including gravity and inviscid limit. *Phys. Rev. Fluids* **3** (9), 091601.

GANÁN-CALVO, A. M. & LOPEZ-HERRERA, J. M. 2019 Capillary soft singularities and ejection: application to the physics of bubble bursting. arXiv:1911.08844.

GEKLE, S. & GORDILLO, J. M. 2010 Generation and breakup of worthington jets after cavity collapse. Part 1. Jet formation. *J. Fluid Mech.* **663**, 293–330.

GEKLE, S., GORDILLO, J. M., VAN DER MEER, D. & LOHSE, D. 2009 High-speed jet formation after solid object impact. *Phys. Rev. Lett.* **102** (3), 034502.

GHABACHE, E., ANTKOWIAK, A., JOSSERAND, C. & SÉON, T. 2014*a* On the physics of fizziness: How bubble bursting controls droplets ejection. *Phys. Fluids* **26** (12), 121701.

GHABACHE, E. & SÉON, T. 2016 Size of the top jet drop produced by bubble bursting. *Phys. Rev. Fluids* **1** (5), 051901.

GHABACHE, É., SÉON, T. & ANTKOWIAK, A. 2014*b* Liquid jet eruption from hollow relaxation. *J. Fluid Mech.* **761**, 206–219.

https://doi.org/10.1017/jfm.2020.851 Published online by Cambridge University Press

GOODRIDGE, C. L., HENTSCHEL, H. G. E. & LATHROP, D. P. 1999 Breaking faraday waves: critical slowing of droplet ejection rates. *Phys. Rev. Lett.* **82** (15), 3062.

GOODRIDGE, C. L., SHI, W. T. & LATHROP, D. P. 1996 Threshold dynamics of singular gravity-capillary waves. *Phys. Rev. Lett.* **76** (11), 1824.

GORDILLO, J. M. 2008 Axisymmetric bubble collapse in a quiescent liquid pool. I. Theory and numerical simulations. *Phys. Fluids* **20** (11), 112103.

GORDILLO, J. M. & RODRÍGUEZ-RODRÍGUEZ, J. 2018 Comment on 'Revision of bubble bursting: universal scaling laws of top jet drop size and speed'. *Phys. Rev. Lett.* **121** (26), 269401.

GORDILLO, J. M. & RODRÍGUEZ-RODRÍGUEZ, J. 2019 Capillary waves control the ejection of bubble bursting jets. *J. Fluid Mech.* **867**, 556–571.

GORDILLO, J. M. & GEKLE, S. 2010 Generation and breakup of worthington jets after cavity collapse. Part 2. Tip breakup of stretched jets. *J. Fluid Mech.* **663**, 331–346.

GOVINDARAJAN, R. 2004 Effect of miscibility on the linear instability of two-fluid channel flow. *Intl J. Multiphase Flow* **30** (10), 1177–1192.

GOVINDARAJAN, R. & NARASIMHA, R. 1999 Low-order parabolic theory for 2D boundary-layer stability. *Phys. Fluids* **11** (6), 1449–1458.

HAMMACK, J. L. & HENDERSON, D. M. 1993 Resonant interactions among surface water waves. *Annu. Rev. Fluid Mech.* **25** (1), 55–97.

HOGREFE, J. E., PEFFLEY, N. L., GOODRIDGE, C. L., SHI, W. T., HENTSCHEL, H. G. E. & LATHROP, D. P. 1998 Power-law singularities in gravity-capillary waves. *Physica* D **123** (1-4), 183–205.

ISMAIL, A. S., GAÑÁN-CALVO, A. M., CASTREJÓN-PITA, J. R., HERRADA, M. A. & CASTREJÓN-PITA, A. A. 2018 Controlled cavity collapse: scaling laws of drop formation. *Soft Matt.* **14** (37), 7671–7679.

JACOBS, J. W. & CATTON, I. 1988 Three-dimensional Rayleigh–Taylor instability. Part 1. Weakly nonlinear theory. *J. Fluid Mech.* **187**, 329–352.

JAMES, A. J., VUKASINOVIC, B., SMITH, M. K. & GLEZER, A. 2003 Vibration-induced drop atomization and bursting. *J. Fluid Mech.* **476**, 1–28.

KANG, Y. J. & CHO, Y. 2019 Gravity–capillary jet-like surface waves generated by an underwater bubble. *J. Fluid Mech.* **866**, 841–864.

KIENTZLER, C. F., ARONS, A. B., BLANCHARD, D. C. & WOODCOCK, A. H. 1954 Photographic investigation of the projection of droplets by bubbles bursting at a water surface. *Tellus* **6** (1), 1–7.

KIM, N. & PARK, H. 2019 Water entry of rounded cylindrical bodies with different aspect ratios and surface conditions. *J. Fluid Mech.* **863**, 757–788.

KRISHNAN, S., HOPFINGER, E. J. & PUTHENVEETTIL, B. A. 2017 On the scaling of jetting from bubble collapse at a liquid surface. *J. Fluid Mech.* **822**, 791–812.

KROON, L. A. M. 2012 On Faraday waves and jets. Master's thesis, University of Twente.

LAI, C.-Y., EGGERS, J. & DEIKE, L. 2018 Bubble bursting: universal cavity and jet profiles. *Phys. Rev. Lett.* **121** (14), 144501.

LAKE, B. M. & YUEN, H. C. 1977 A note on some nonlinear water-wave experiments and the comparison of data with theory. *J. Fluid Mech.* **83** (1), 75–81.

LIGER-BELAIR, G., CILINDRE, C., GOUGEON, R. D., LUCIO, M., GEBEFÜGI, I., JEANDET, P. & SCHMITT-KOPPLIN, P. 2009 Unraveling different chemical fingerprints between a champagne wine and its aerosols. *Proc. Natl Acad. Sci. USA* **106** (39), 16545–16549.

LONGUET-HIGGINS, M. S. 1978 The instabilities of gravity waves of finite amplitude in deep water I. Superharmonics. *Proc. R. Soc. Lond.* A **360** (1703), 471–488.

LONGUET-HIGGINS, M. S. 1983 Bubbles, breaking waves and hyperbolic jets at a free surface. *J. Fluid Mech.* **127**, 103–121.

LONGUET-HIGGINS, M. S. 1994 Inertial shocks in surface waves and collapsing bubbles. In *Bubble Dynamics and Interface Phenomena*, pp. 383–396. Springer.

MACINTYRE, F. 1972 Flow patterns in breaking bubbles. *J. Geophys. Res.* **77** (27), 5211–5228.

MACK, L. R. 1962 Periodic, finite-amplitude, axisymmetric gravity waves. *J. Geophys. Res.* **67** (2), 829–843.

MAT 2018 *MATLAB Version 9.4.0.813654 (R2018a)*. The Mathworks, Inc.

https://doi.org/10.1017/jfm.2020.851 Published online by Cambridge University Press

McGoldrick, L. F. 1970 On Wilton's ripples: a special case of resonant interactions. *J. Fluid Mech.* **42** (1), 193–200.

Milgram, J. H. 1969 The motion of a fluid in a cylindrical container with a free surface following vertical impact. *J. Fluid Mech.* **37** (3), 435–448.

Morton, D., Rudman, M. & Jong-Leng, L. 2000 An investigation of the flow regimes resulting from splashing drops. *Phys. Fluids* **12** (4), 747–763.

Natarajan, R. & Brown, R. A. 1986 Quadratic resonance in the three-dimensional oscillations of inviscid drops with surface tension. *Phys. Fluids* **29** (9), 2788–2797.

Penney, W. G., Price, A. T., Martin, J. C., Moyce, W. J., Penney, W. G., Price, A. T. & Thornhill, C. K. 1952 Part II. Finite periodic stationary gravity waves in a perfect liquid. *Phil. Trans. R. Soc. Lond.* A **244** (882), 254–284.

Popinet, S. 2003 Gerris: a tree-based adaptive solver for the incompressible Euler equations in complex geometries. *J. Comput. Phys.* **190** (2), 572–600.

Popinet, S. 2009 An accurate adaptive solver for surface-tension-driven interfacial flows. *J. Comput. Phys.* **228** (16), 5838–5866.

Popinet, S. 2018 Numerical models of surface tension. *Annu. Rev. Fluid Mech.* **50**, 49–75.

Popinet, S. 2020 Basilisk flow solver and PDE library. http://basilisk.fr, [Online; accessed 20-January-2020].

Price, W. G. & Penneyand, A. T. 1952 Finite periodic stationary gravity waves in a perfect fluid. Part 2. *Phil. Trans. R. Soc. Lond.* A **244**, 254.

Prosperetti, A. & Oguz, H. N. 1993 The impact of drops on liquid surfaces and the underwater noise of rain. *Annu. Rev. Fluid Mech.* **25** (1), 577–602.

Raja, D. K., Das, S. P. & Hopfinger, E. J. 2019 On standing gravity wave-depression cavity collapse and jetting. *J. Fluid Mech.* **866**, 112–131.

Ray, B., Biswas, G. & Sharma, A. 2015 Regimes during liquid drop impact on a liquid pool. *J. Fluid Mech.* **768**, 492–523.

van Rijn, C. J. M. 2018 Emanating jets as shaped by surface tension forces. *Langmuir* **34** (46), 13837–13844.

Scardovelli, R. & Zaleski, S. 1999 Direct numerical simulation of free-surface and interfacial flow. *Annu. Rev. Fluid Mech.* **31** (1), 567–603.

Schwartz, L. W. & Whitney, A. K. 1981 A semi-analytic solution for nonlinear standing waves in deep water. *J. Fluid Mech.* **107**, 147–171.

Segur, H. & Stewart, A. 2020 Lecture 4: Zhakharov formulation of water waves. https://gfd.whoi.edu/wp-content/uploads/sites/18/2018/03/lecture4-harvey_136525.pdf, online; accessed 29 February 2020.

Séon, T. & Liger-Belair, G. 2017 Effervescence in champagne and sparkling wines: from bubble bursting to droplet evaporation. *Eur. Phys. J.: Spec. Top.* **226** (1), 117–156.

Shi, W. T., Goodridge, C. L. & Lathrop, D. P. 1997 Breaking waves: bifurcations leading to a singular wave state. *Phys. Rev.* E **56** (4), 4157.

Shin, J. & McMahon, T. A. 1990 The tuning of a splash. *Phys. Fluids* A **2** (8), 1312–1317.

Singh, M., Farsoiya, P. K. & Dasgupta, R. 2019 Test cases for comparison of two interfacial solvers. *Intl J. Multiphase Flow* **115**, 75–92.

Strutt, J. W. 1915 Deep water waves, progressive or stationary, to the third order of approximation. *Proc. R. Soc. Lond.* A **91** (629), 345–353.

Taylor, G. I. 1953 An experimental study of standing waves. *Proc. R. Soc. Lond.* A **218** (1132), 44–59.

Thoroddsen, S. T., Etoh, T. G. & Takehara, K. 2007 Microjetting from wave focusing on oscillating drops. *Phys. Fluids* **19** (5), 052101.

Thoroddsen, S. T., Takehara, K., Nguyen, H. D. & Etoh, T. G. 2018 Singular jets during the collapse of drop-impact craters. *J. Fluid Mech.* **848**, R3.

Tjan, K. K. & Phillips, W. R. C. 2007 On impulsively generated inviscid axisymmetric surface jets, waves and drops. *J. Fluid Mech.* **576**, 377–403.

Truscott, T. T., Epps, B. P. & Belden, J. 2014 Water entry of projectiles. *Annu. Rev. Fluid Mech.* **46**, 355–378.

https://doi.org/10.1017/jfm.2020.851 Published online by Cambridge University Press

TSAI, C., MAO, R., TSAI, S., SHAHVERDI, K., ZHU, Y., LIN, S., HSU, YU.-H., BOSS, G., BRENNER, M., MAHON, S., *et al.* 2017 Faraday waves-based integrated ultrasonic micro-droplet generator and applications. *Micromachines* **8** (2), 56.

VERON, F. 2015 Ocean spray. *Annu. Rev. Fluid Mech.* **47**, 507–538.

VIOLA, F., BRUN, P.-T. & GALLAIRE, F. 2018 Capillary hysteresis in sloshing dynamics: a weakly nonlinear analysis. *J. Fluid Mech.* **837**, 788–818.

WILTON, J. R. 1915 LXXII. On ripples. *Lond. Edinb. Dubl. Phil. Mag. J. Sci.* **29** (173), 688–700.

WOODCOCK, A. H., KIENTZLER, C. F., ARONS, A. B. & BLANCHARD, D. C. 1953 Giant condensation nuclei from bursting bubbles. *Nature* **172** (4390), 1144–1145.

WORTHINGTON, A. M. & COLE, R. S. 1897 V. Impact with a liquid surface, studied by the aid of instantaneous photography. *Phil. Trans. R. Soc. Lond.* A **189**, 137–148.

WORTHINGTON, A. M. & COLE, R. S. 1900 IV. Impact with a liquid surface studied by the aid of instantaneous photography. Paper II. *Phil. Trans. R. Soc. Lond.* A **194** (252–261), 175–199.

YAMAMOTO, K., MOTOSUKE, M. & OGATA, S. 2018 Initiation of the worthington jet on the droplet impact. *Appl. Phys. Lett.* **112** (9), 093701.

YUKISADA, R., KIYAMA, A., ZHANG, X. & TAGAWA, Y. 2018 Enhancement of focused liquid jets by surface bubbles. *Langmuir* **34** (14), 4234–4240.

ZAKHAROV, V. E. 1968 Stability of periodic waves of finite amplitude on the surface of a deep fluid. *J. Appl. Mech. Tech. Phys.* **9** (2), 190–194.

ZEFF, B. W., KLEBER, B., FINEBERG, J. & LATHROP, D. P. 2000 Singularity dynamics in curvature collapse and jet eruption on a fluid surface. *Nature* **403** (6768), 401.

https://doi.org/10.1017/jfm.2020.851 Published online by Cambridge University Press